Chapter 5. Array of Star Spirals

The star spiral was introduced in the previous chapter and it compared well with the circular Archimedean spiral. This chapter will examine the star spiral in an array environment. First, an infinite array of star spirals will be compared to an infinite array of circular spirals. Analysis Software of Infinite Arrays (ASIA), developed at the Virginia Tech Antenna Group, will be used to do the comparison. Input impedance versus frequency and the scan performance of the elements will be investigated. Secondly, the star spiral will be used in the Wideband Array with Variable Element Sizes (WAVES). The star spiral was originally developed to overcome the performance gap observed in the WAVES arrays of Chapter 3, which used circular Archimedean spiral elements. This chapter will demonstrate the operation of the linear WAVES array using the star spiral and it will also investigate the scan performance of a linear WAVES array of star spirals. An extension of the 2-octave linear WAVES array to 3-octaves will also be presented. Simulations and measurements verify 3-octave performance. Lastly, alternative array geometries will be presented that take advantage of the unique packing features of the star spiral.

5.1 Infinite Array of Spirals

The infinite array analysis of the star spiral will be used to validate the performance of the star spiral in an array environment. It is desirable for the star spiral to show significant size reduction and to demonstrate similar scan performance compared to the circular spiral. The infinite array simulations will be performed using ASIA. Because the computation time for the optimum star spiral presented in the previous chapter is so great in ASIA, a non-optimum, smaller star spiral was used to make the simulation practical. The star spiral used in ASIA is shown in Fig. 5.1. Each arm of the spiral was modeled as a flat strip and the blue rectangle marks the source region. The parameters of the star spiral are $r_2 = 0.0161m$, $N = 6$ turns, and $v = 2$. The equivalent circular spiral, shown in Fig. 5.2, has an outer radius of $r_2 = 0.0198m$ and the inter-element spacing modeled in ASIA is $0.0415m$. The input impedance of the star spiral and the equivalent circular spiral is shown in Fig. 5.3. The plot shows that both the

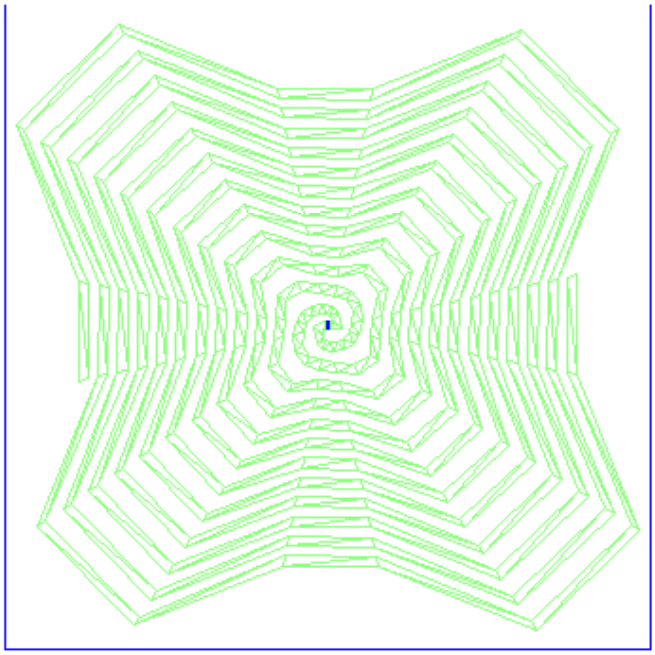

Figure 5.1 Geometry of star spiral used in ASIA simulations.

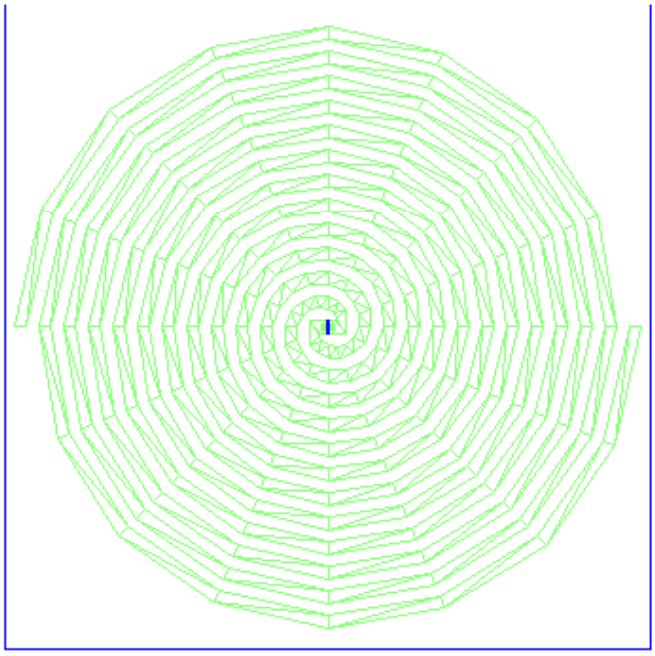

Figure 5.2 Geometry of circular spiral used in ASIA simulations.

star spiral and the circular spiral have nearly constant input impedance over a wide frequency range. Note that the ASIA model gives an input impedance of approximately 240Ω, which is a little higher than expected. The VSWR of both spirals, referenced to 240Ω, is plotted in Fig. 5.4. The low frequency cutoff of the circular spiral is 2290 MHz and the low frequency cutoff of the star spiral is 1985 MHz, which gives a size reduction of 13.3% in the infinite array environment. For comparison, both spirals were also simulated as single elements in NEC4 using the same techniques outlined in previous chapters. From NEC4, the low frequency cutoff of the star spiral is 2314 MHz and the low frequency cutoff of the circular spiral is 2696 MHz for a size reduction of 14.2%. The comparison shows that the array performance of the spirals is similar to its single element performance.

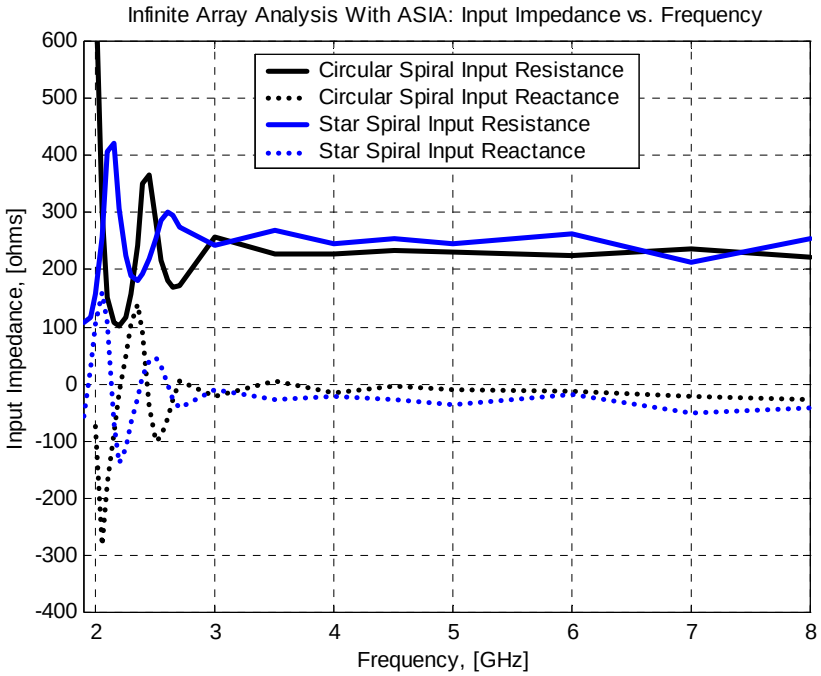

Figure 5.3 ASIA simulation of input impedance versus frequency for star spiral and circular spiral.

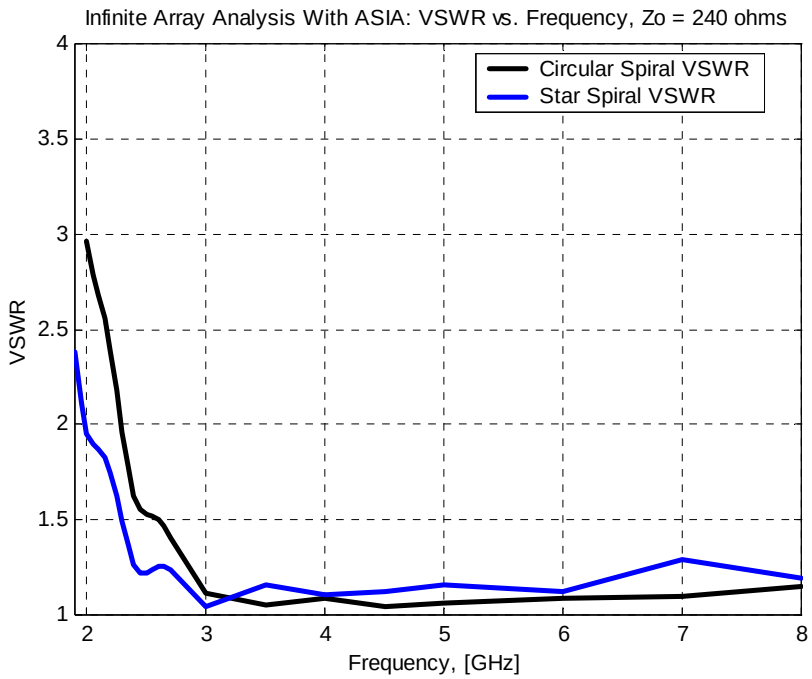

Figure 5.4 ASIA simulation of VSWR versus frequency for star spiral and circular spiral.

Since array scanning is desirable for many applications it is important to determine if the unique shape of the star spiral has any effect on the scan performance. Frequencies of 3000 MHz and 3500 MHz were chosen to examine the scan performance of the two spiral elements. These frequencies are in the range where both spirals have good impedance and pattern performance. Using ASIA, both arrays were scanned in theta for $\phi = 0°$ and $\phi = 45°$. The input impedance for both spirals versus theta scan angle is plotted in Fig. 5.5 for 3000 MHz and in Fig. 5.6 for 3500 MHz. Similarly, the gain loss for both frequencies is presented in Fig. 5.7 and Fig. 5.8, respectively. The gain loss, as defined here, is equal to $1-|\Gamma|^2$, where Γ is the reflection coefficient, which is referenced to the input impedance for zero scan. The gain loss is an indicator of the mutual coupling effects on the realized array gain due to scanning the beam. It is desirable for the input impedance to remain fairly constant as the array is scanned. Fig. 5.5 and Fig. 5.6 show that the input impedance for both spirals is relatively stable up to a 40° scan angle. However, in terms of gain loss, both the star spiral and circular spiral have less than a 1dB gain loss for theta scan angles

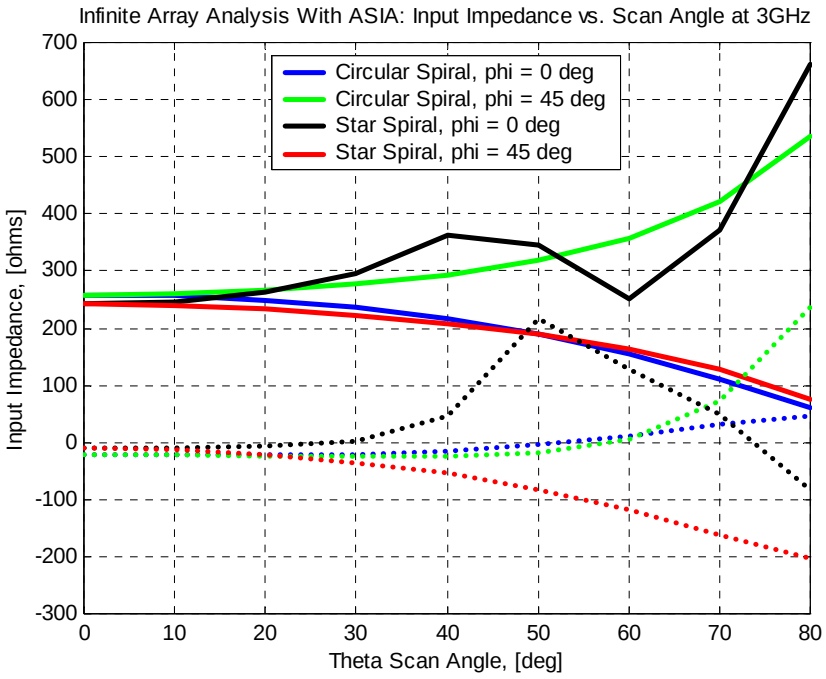

Figure 5.5 ASIA simulation of input impedance versus theta scan angle for the star spiral and the circular spiral at 3000 MHz.

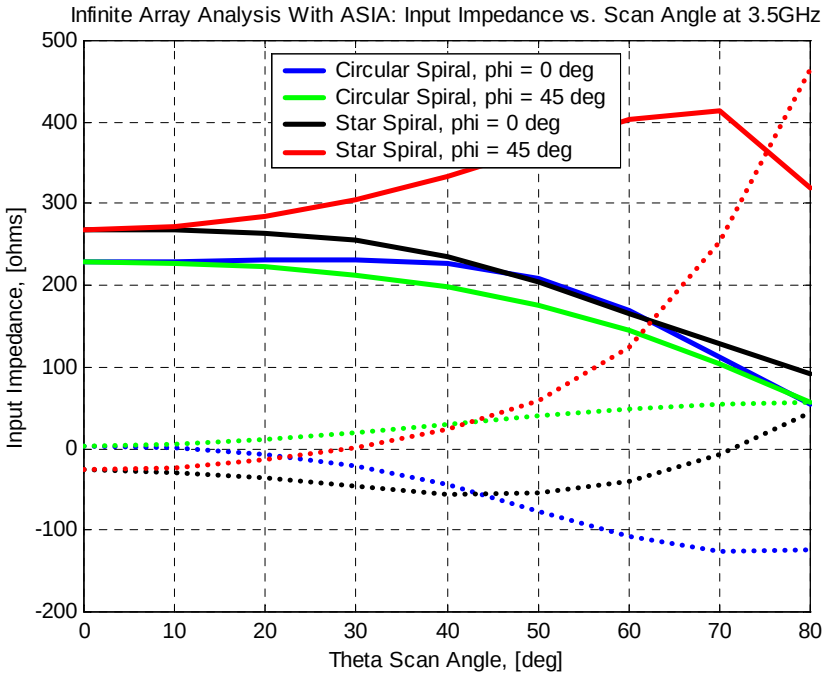

Figure 5.6 ASIA simulation of input impedance versus theta scan angle for the star spiral and the circular spiral at 3500 MHz.

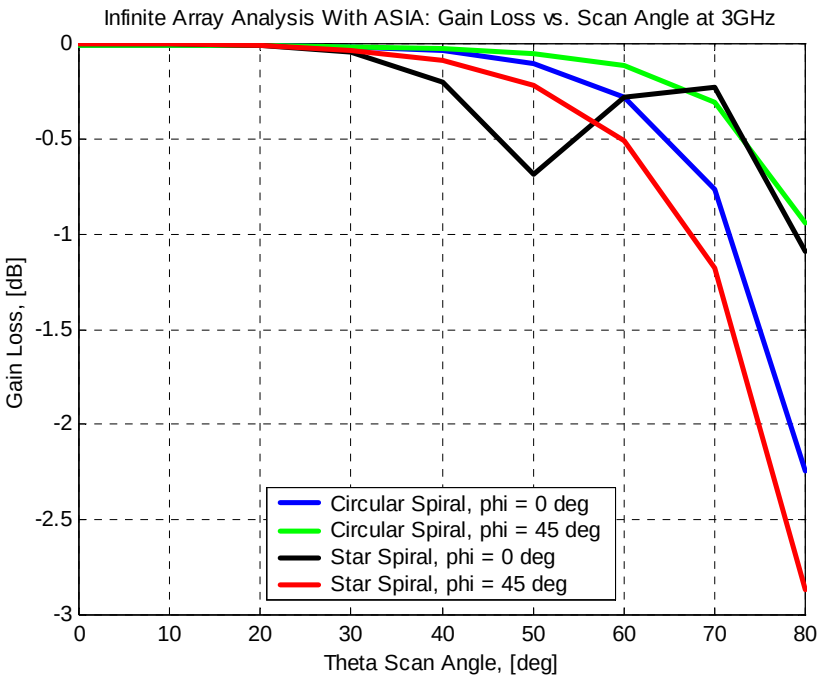

Figure 5.7 ASIA simulation of gain loss versus theta scan angle for the star spiral and the circular spiral at 3000 MHz.

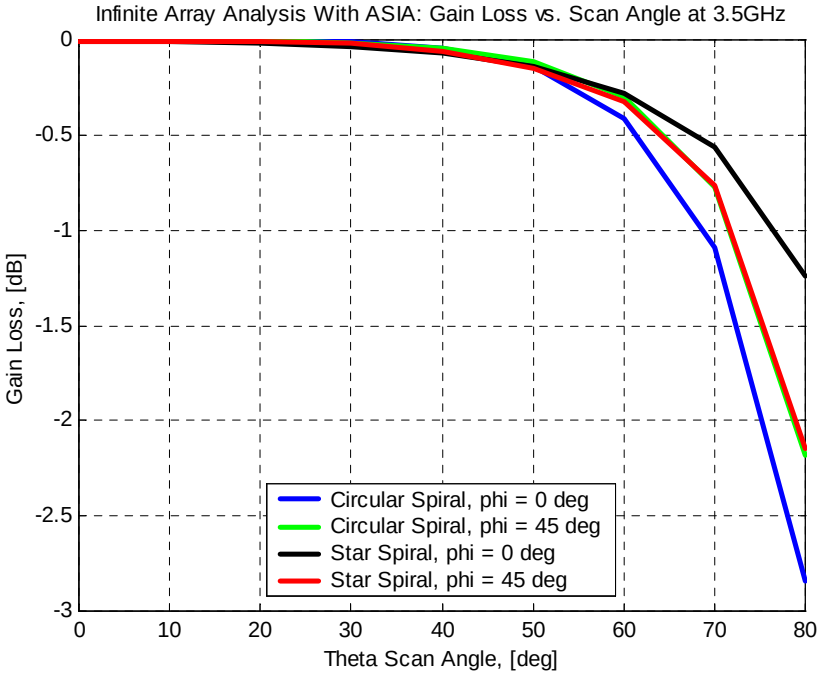

Figure 5.8 ASIA simulation of gain loss versus theta scan angle for the star spiral and the circular spiral at 3500 MHz.

less than 65° as seen in Fig. 5.7 and Fig. 5.8. These plots show that the unique shape of the star spiral does not significantly affect the scan performance of an array compared to an array of circular Archimedean spirals.

5.2 Linear WAVES Array of Star Spirals

The linear WAVES array was first presented in Chapter 3 where circular Archimedean spiral elements were used. The array was shown to have a performance gap between 1960 MHz where the first grating lobe appears and 2275 MHz where the smaller, second octave element becomes active. The star spiral was designed to eliminate the performance gap in the array. Fig. 5.9 shows the same linear WAVES array of Chapter 3 where the circular spiral elements have been replaced with star spiral elements.

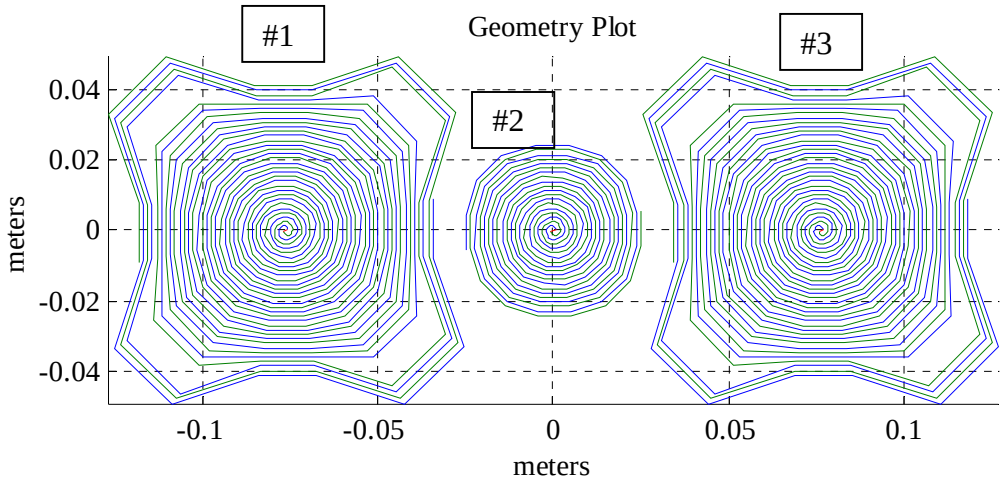

Figure 5.9 Three-element linear WAVES array of star spirals.

The linear extent of each star spiral is the same as its comparable circular spiral used in Chapter 3. The parameters of the larger star spiral are $r_2 = 0.0429m$, $N = 16$ turns, $dr = 0.00009$, $taper = 260$, $trans = 174$, and $v = 14$, which are the same as the optimum spiral presented in Table 4.4 and Fig. 4.18. The smaller spiral has the same parameter as the larger spiral except $r_2 = 0.025469m$ and $N = 9.5$ turns. The VSWR performance of the array of Fig. 5.9 is shown in Fig. 5.10. According to the WAVES theory presented in Chapter 3 this array is designed to operate from 1000 MHz to 4000 MHz. Fig. 5.10(a)

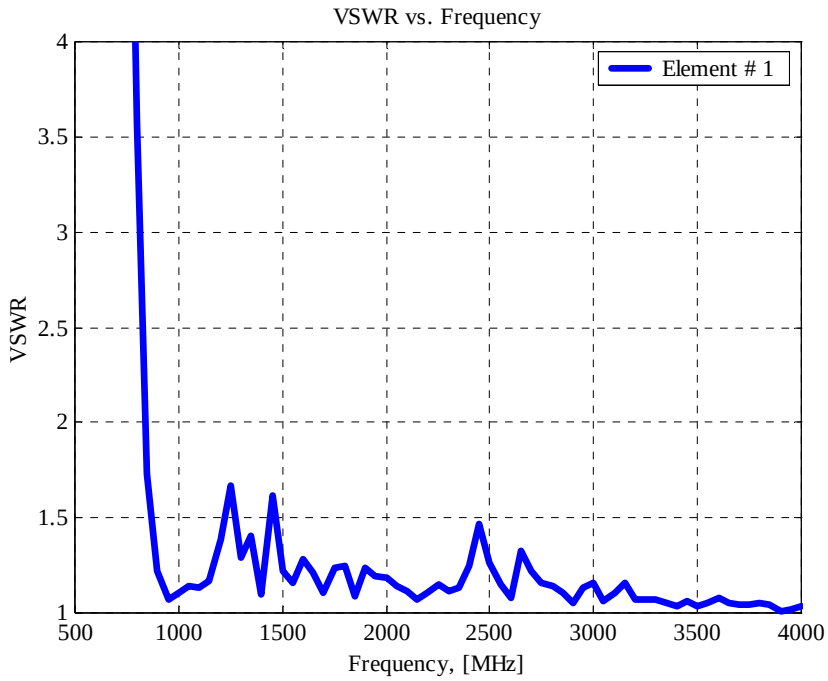

(a) Only larger spirals active.

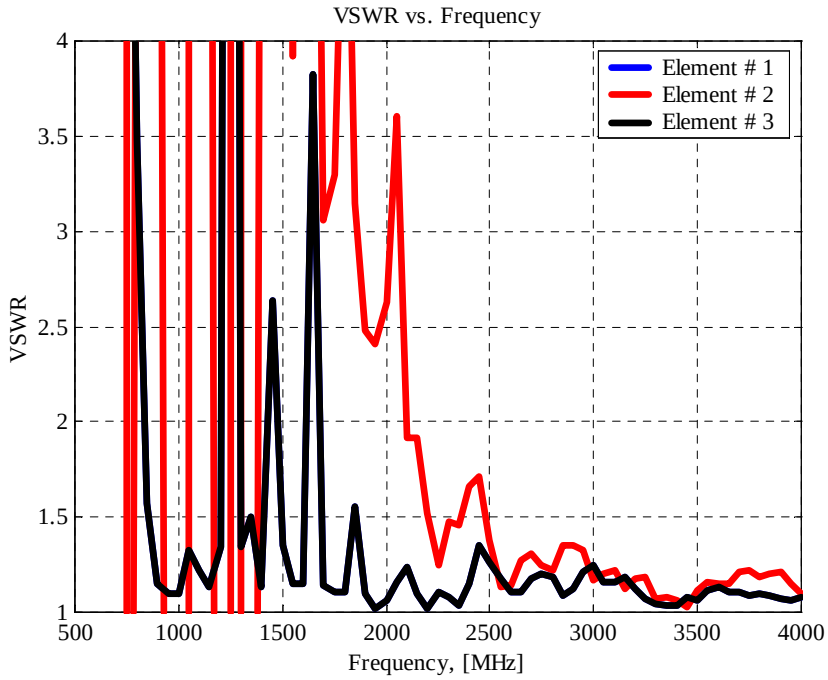

(b) All elements active. (Elements #1 and #3 are identical)

Figure 5.10 VSWR plot of 3-element linear WAVES array of star spirals. Geometry is comparable to 3-element linear WAVES array of circular spirals from Chapter 3.

shows that satisfactory performance begins at 843 MHz where the larger spirals have a VSWR less than 2:1. The first grating lobe, computed from inter-element spacing, appears at 1960 MHz and from Fig. 5.10(b) it can be seen the smaller element does not radiate efficiently until about 2098 MHz. In the simulation, the difference between an active an inactive element is the presence of the voltage source. In practice, this is equivalent to shorting the two arms together.

As in Chapter 3 a performance gap is observed between the lower and higher octaves, but the unique shape of the star spiral allows this performance problem to be overcome. The performance gap can be eliminated in two ways. The larger spirals can be moved closer together to reduce the inter-element spacing and delay the appearance of the grating lobe until about 2100 MHz where the smaller spiral becomes active. The second approach, shown in Fig. 5.11, is to increase the diameter of the smaller element,

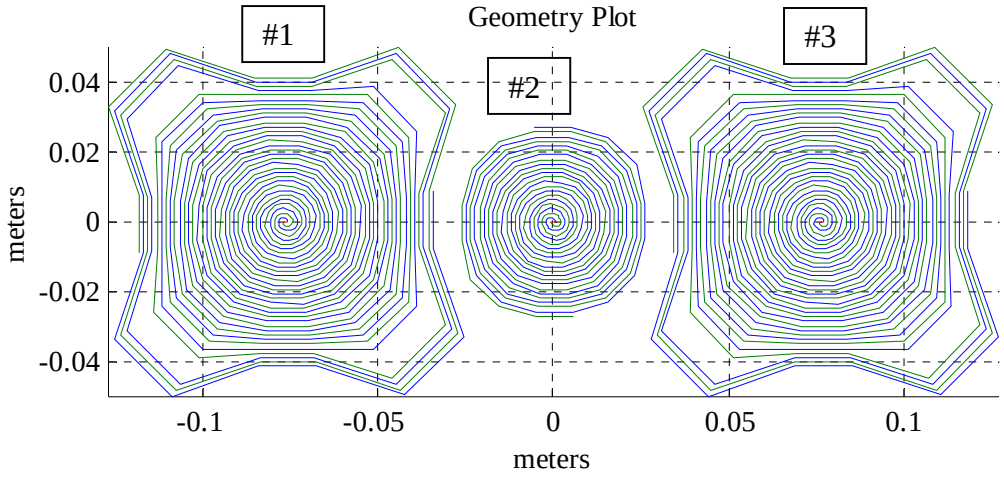

Figure 5.11 Improved 3-element linear WAVES array of star spirals.

which reduces the low frequency cutoff of the smaller element to below 1960 MHz. The parameters of the new smaller spiral are $r_2 = 0.027479m$ and $N = 10.25$ turns. An equivalent (in terms of the linear extent of each spiral) 3-element linear WAVES array of circular spirals is shown in Fig. 5.12. It can be seen that if circular spirals were used the elements would overlap, particularly when the spirals were actually constructed using strips instead of the wires as shown in Fig. 5.12. The VSWR performance of the improved linear array of Fig. 5.11 is plotted in Fig. 5.13. The low frequency cutoffs of

the improved array are 840 MHz for the larger spiral and 1924 MHz for the smaller element. The improved linear array of star spirals has completely eliminated the performance gap and also improved the low frequency response of the array. The array operates from 840 MHz to 3920 MHz where the second grating lobe appears, which is a functional bandwidth of 4.67:1. So, use of the star spiral has improved the linear WAVES array performance from a 4:1 bandwidth with a hole in the coverage to a fully functioning array with greater than 2 octaves of bandwidth.

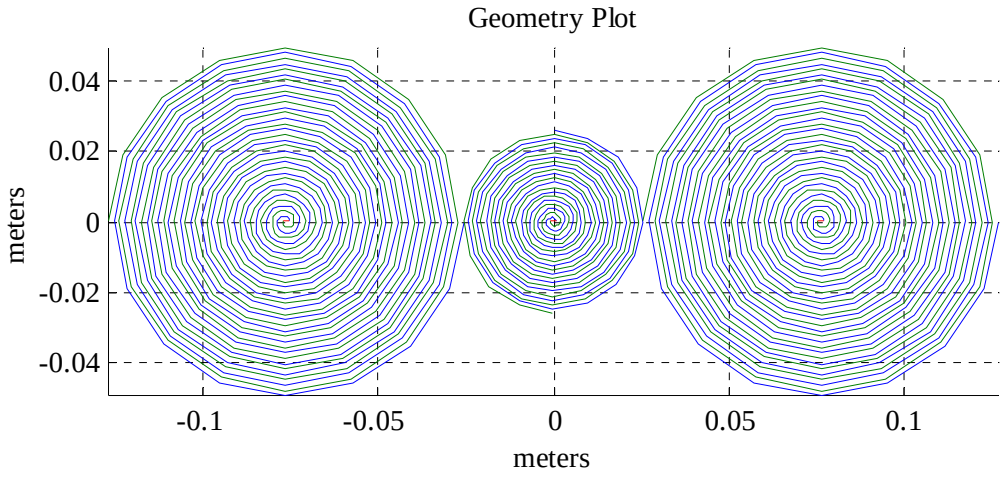

Figure 5.12 Equivalent 3-element linear WAVES array of circular spirals.

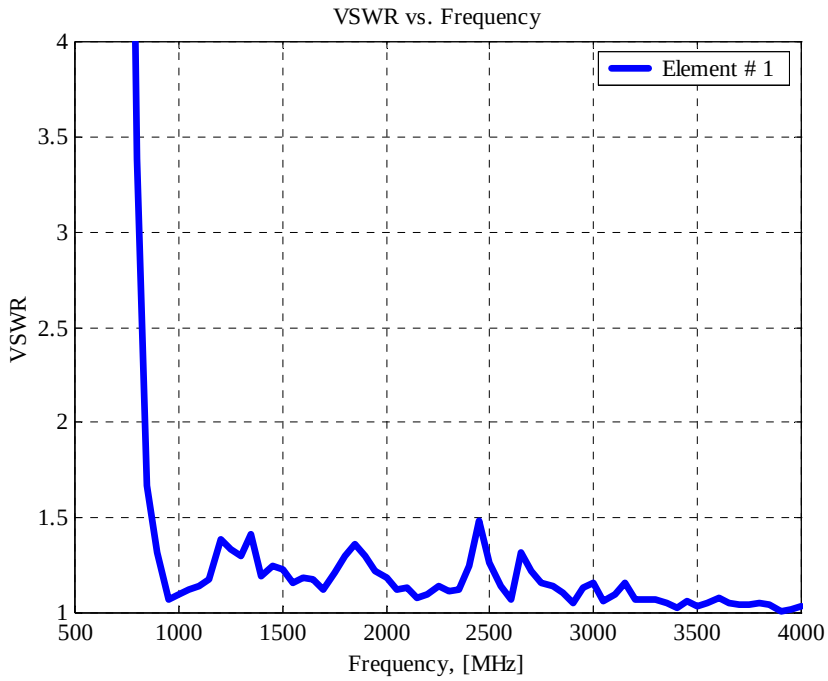

(a) Only larger spirals active.

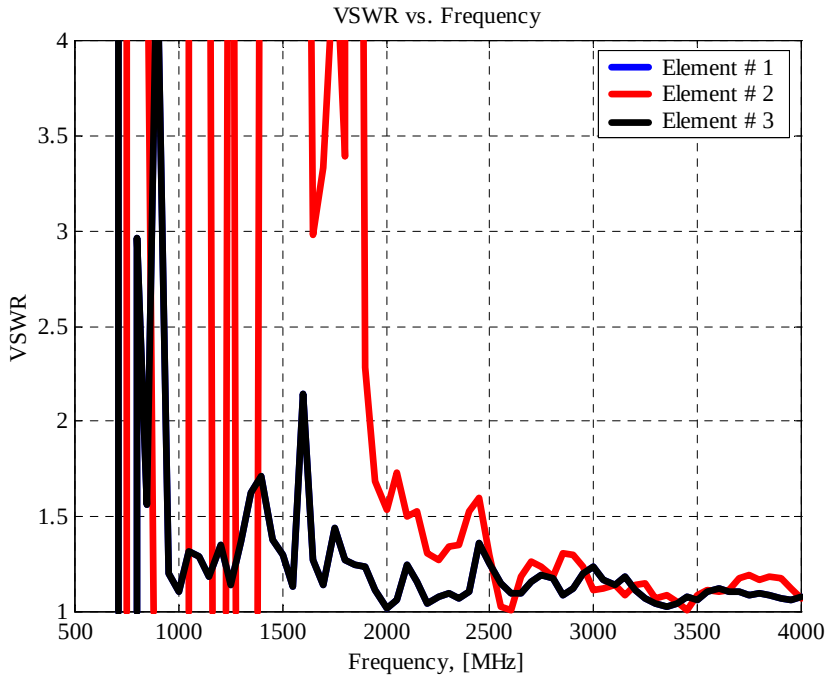

(b) All elements active. (Elements #1 and #3 are identical)

Figure 5.13 Simulated VSWR plot of improved 3-element linear WAVES array of star spirals of Fig. 5.11.

5.3 Three-Octave WAVES Array

The previous section demonstrated the operation of a linear WAVES array. The linear array can be easily extended to a planar array similar to that presented in Chapter 3. This section will show a basic extension of the WAVES array to 3-octaves of coverage. The geometry is shown in Fig. 5.14. The dimensions of the spirals from largest to smallest are $r_2 = 0.0429m$ and $N = 16$ turns, $r_2 = 0.02949m$ and $N = 11$ turns, and $r_2 = 0.01609m$ and $N = 6$ turns. All of the spirals have $dr = 0.00009$, $taper = 260$, $trans = 174$, and $v = 14$. The size of the three spirals was chosen such that the VSWR of the array is better than 2:1 over the entire frequency band. Since the measurement setup available was limited to a maximum of eight elements, the array geometry of Fig. 5.14 was chosen to allow for the array to be constructed and tested. The larger spiral has a low frequency cutoff of 849 MHz, the medium spiral has a low frequency cutoff of 1680 MHz, and the smallest spiral has a low frequency cutoff of 3255 MHz. The inter-element

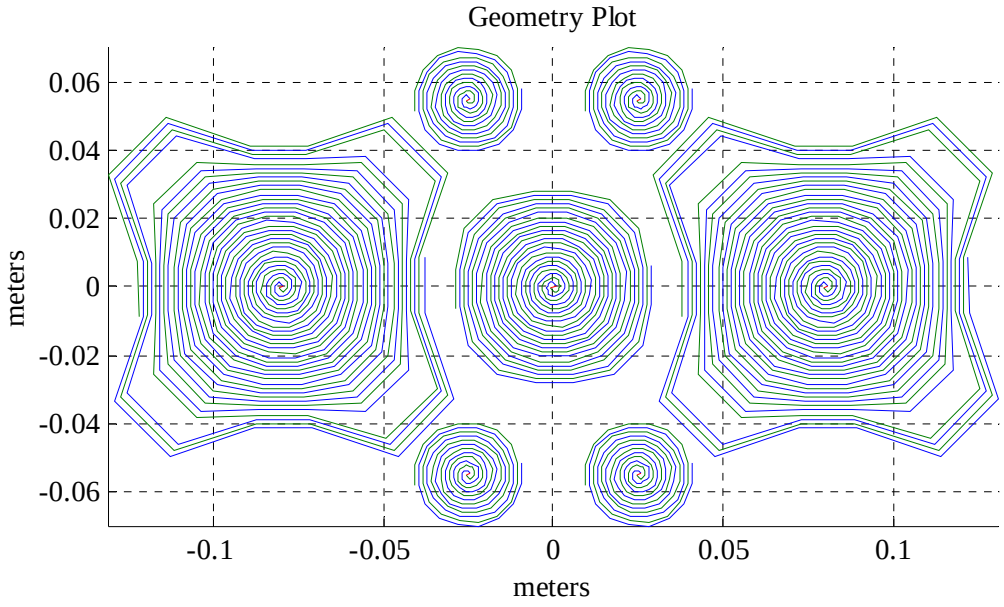

Figure 5.14 Geometry of 3-octave WAVES array of star spirals.

spacing is designed so that the first octave grating lobe appears at 1875 MHz, the second octave grating lobe appears at 3750 MHz, and the third octave grating appears around

8000 MHz. The star spiral elements are designed so that the respective element becomes active before the grating lobe appears to prevent any gaps in the array performance.

The array that was built and tested is shown in Fig. 5.15. The array was printed on RT/Duroid 5880. A 24”x24”x4.5” piece of absorber was placed approximately 1” behind the array to reduce radiation from the feed region, seen in Fig. 5.15(b), and to block reflections from the AUT positioner. Each spiral was fed with a Y-feed made from 0.118” coax. The feeds can be seen in Fig. 5.15. The proper phase for each arm of the spirals was achieved by using a 180° hybrid that fed two 8-way power dividers. The output of the first power divider was connected to one arm of the Y-shaped feed and the output of the second power divider was connected to the other arm of the Y-shaped feed for each spiral. The measured insertion loss of the hybrid and power dividers used in the measurements is shown in Fig. 5.16.

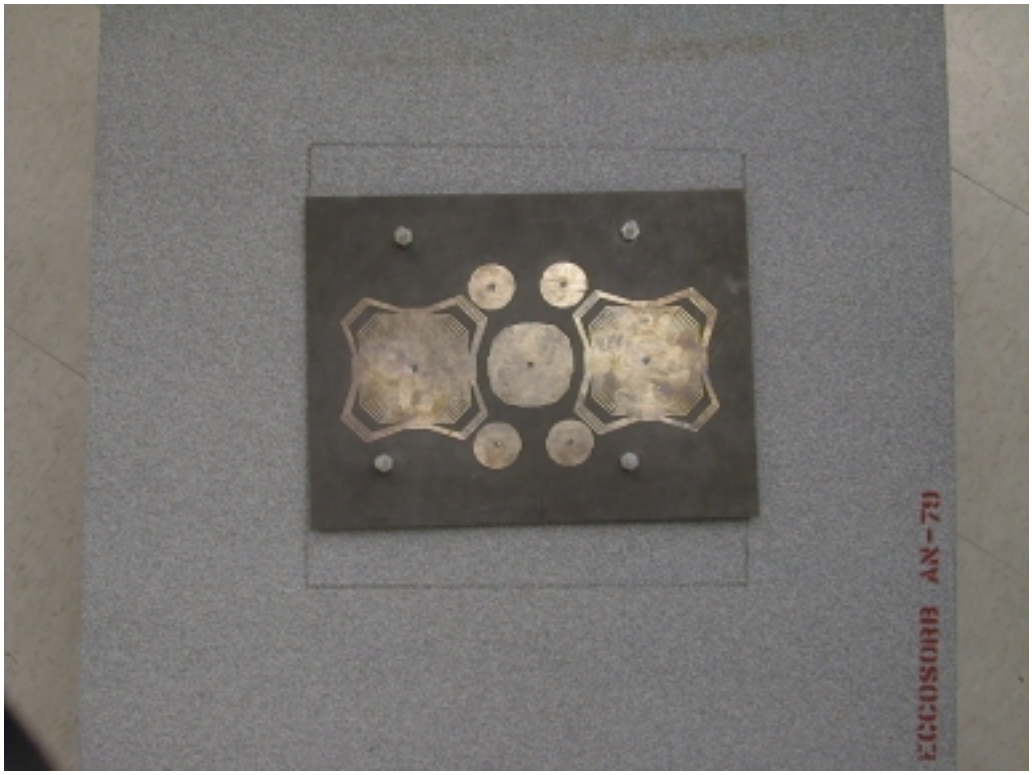

(a) Top view.

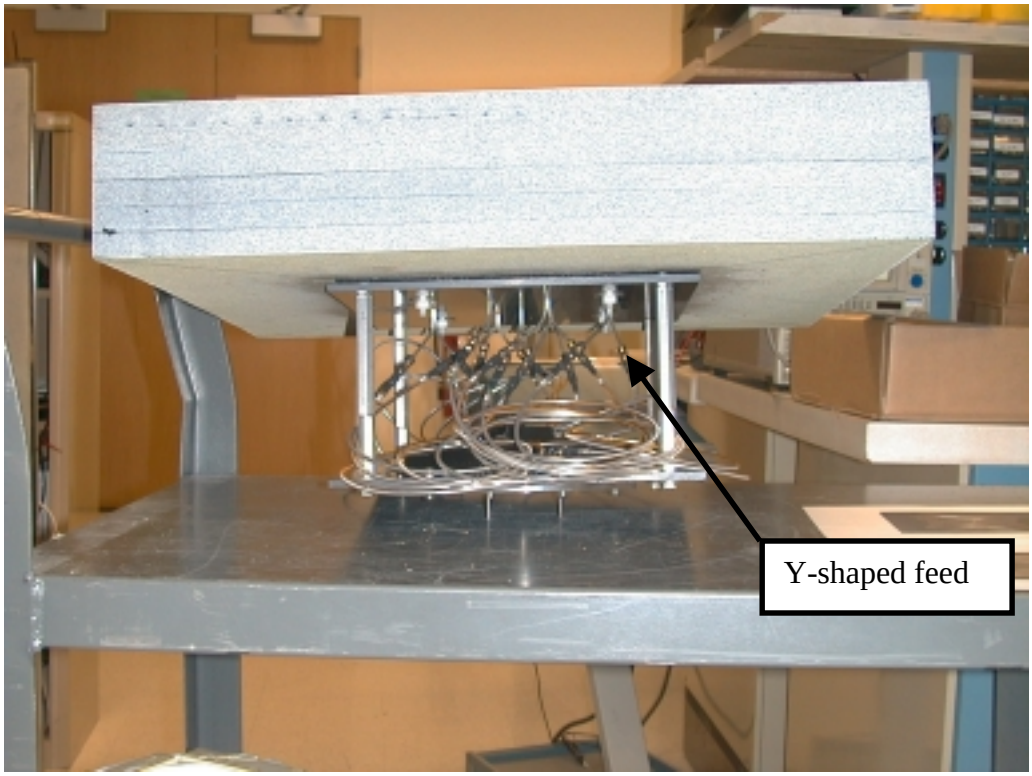

(b) Side View.

Figure 5.15 Geometry of measured 3-octave WAVES array of star spirals.

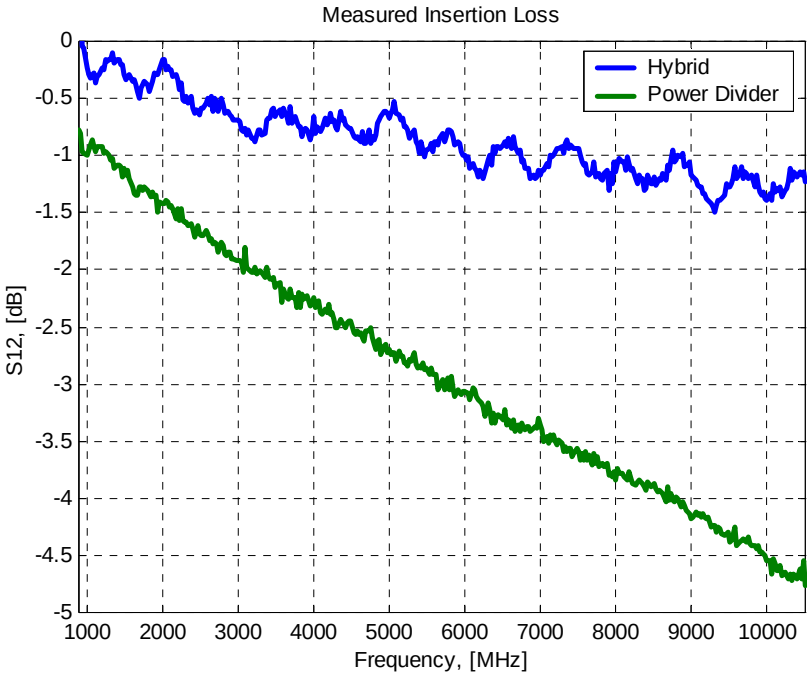

Figure 5.16 Measured hybrid and 8-way power divider insertion loss.

In general the measured performance of the 3-octave array matched very well with the simulated results. The gain of the 3-octave array is as straightforward to determine as for the single element. Various gain curves are plotted in Fig. 5.17. The black curve is the raw measured gain data, but the measurement setup has many loss mechanisms that can be improved or eliminated if the array were manufactured. The red curve is the gain with the hybrid and power divider losses subtracted out, and the blue curve also has the impedance mismatch accounted for. The total impedance mismatch is shown in Fig. 5.18. The mismatch is computed from the simulated VSWR for the entire array referenced to 188Ω.

The mismatch is based on all 7 star spiral elements being active over the entire frequency band. This is different from previous WAVES simulations presented in this dissertation where the elements were not excited when the array was operating out of the spirals active frequency band. Once again this was done for practical reasons, because it was more practical to measure the array with all the elements excited. Also, it makes the WAVES array concept more attractive if the elements do not need to be switched on and off depending on the frequency. Fig. 5.17 shows that the measured gain, with the losses accounted for, matches very well with the simulated gain over most of the frequency range.

Fig. 5.17 also shows the calculated gain of an aperture antenna with the equivalent area of the 3-octave WAVES array. A square aperture that would enclose the array has dimensions of 0.26 x 0.14 meters. The aperture efficiency was assumed be 80%. The gain of the equivalent aperture was determined using $G = \varepsilon_{ap} \frac{4\pi}{\lambda^2} Area$. The gain of the aperture is greater than the 3-octave WAVES array except at the low end of the frequency band. However, the WAVES array has a fairly flat gain response over the entire band, which can be an advantage for applications. The flat gain response indicates a more uniform pattern over the frequency range than the equivalent aperture would have. The lightweight and low profile nature of the 3-octave WAVES array presents a big advantage over an aperture antenna, such as a reflector. For wideband applications where a low profile antenna system is more important than maximizing gain, the WAVES array is an attractive alternative to a multi-feed reflector antenna system.

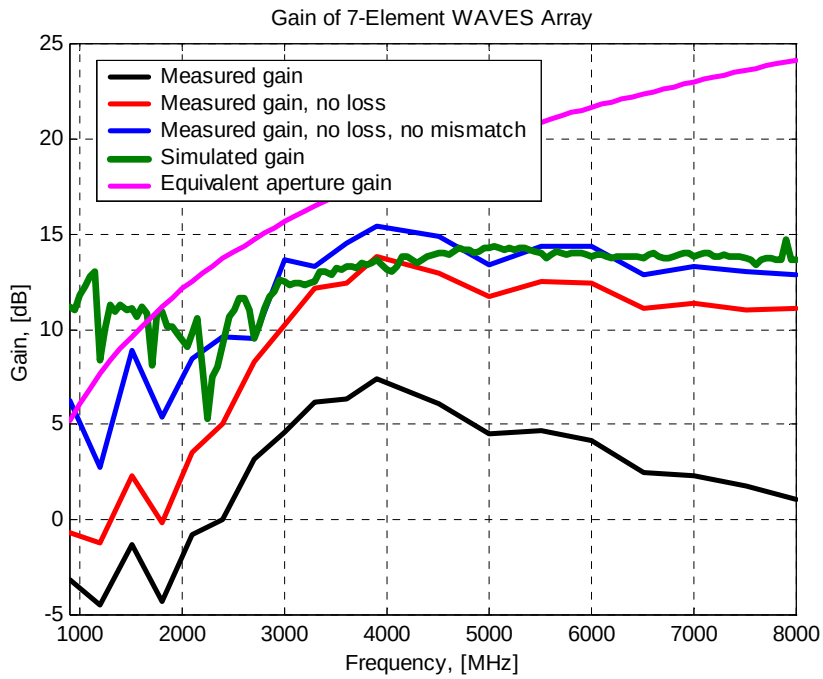

Figure 5.17 Comparison of measured gain to simulated data for 7-element WAVES array. Loss includes the hybrid and 8-way power divider insertion loss and mismatch is total mismatch based on simulated element impedance.

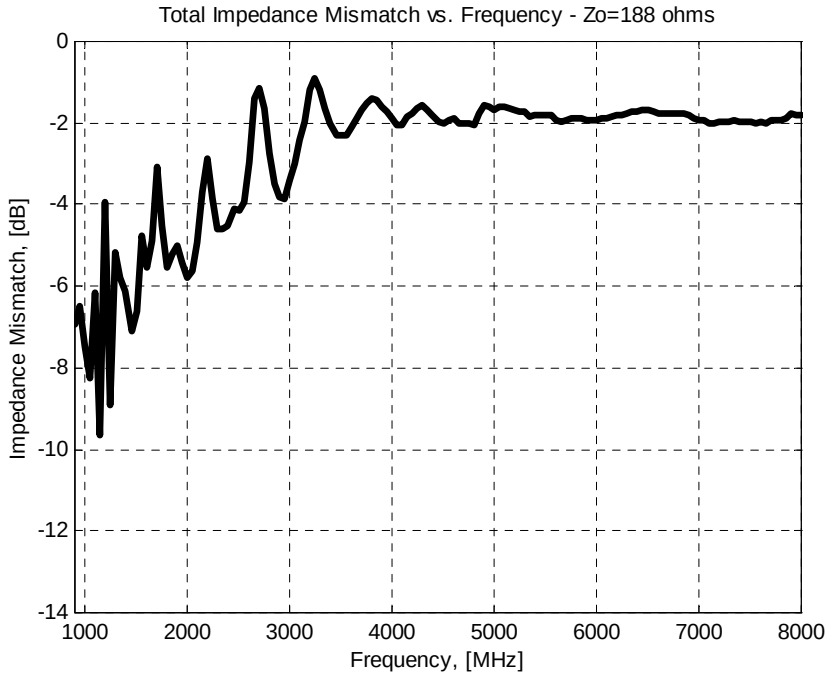

Figure 5.18 Simulated total impedance mismatch for 7-element WAVES array. All 7 elements are active over the entire frequency band.

The measured boresight axial ratio of the 3-octave array versus frequency is shown in Fig. 5.19. As with the previous axial ratio measurements of the star spiral the axial ratio of the array is marginal over about half of the frequency band, particularly at low end of the band. It is well known that the axial ratio of spiral antennas is poor at the low end of its operating band so it is to be expected that the axial ratio of the array would be affected as the smaller elements start to radiate. The axial ratio can be improved by using a 4-arm star spiral element.

The far-field patterns versus theta angle from boresight of the 3-octave WAVES array are plotted in Fig. 5.20 for selected frequencies from 900 MHz to 8000 MHz. The measured patterns compare very well with the simulated results for most of the frequencies. At a few of the lower frequencies there is some discrepancy, which is probably due to the interaction of the radiating spiral with the out of band spirals. Similarly the axial ratio patterns versus theta for the same frequencies are plotted in Fig. 5.21. The same general trends that were observed for the radiation patterns apply to the axial ratio patterns. The agreement between the measured results and the simulated results is best at the high end of the frequency band because all of the different element sizes are operating within their appropriate frequency ranges. Both the far-field and axial ratio patterns become noisier with increasing frequency, which is due to coaxial losses in the measurement setup. To summarize all of the measurements, the 3-octave WAVES array operates from about 850 MHz, where the largest star spiral becomes operational, to about 7000 MHz, where the third octave grating lobe appears, which is an 8.2:1 bandwidth.

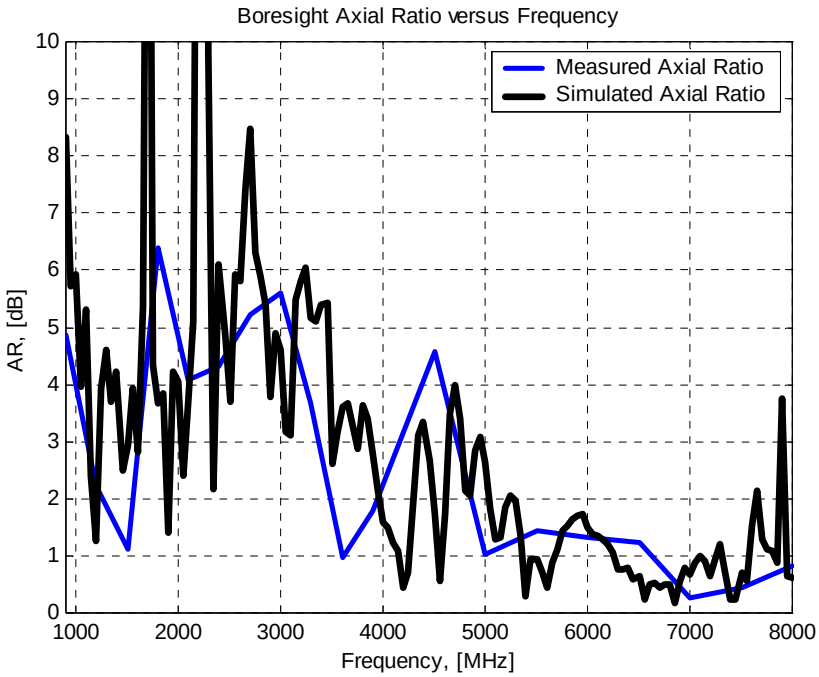

Figure 5.19 Comparison of measured boresight axial ratio to simulated data for 7-element WAVES array.

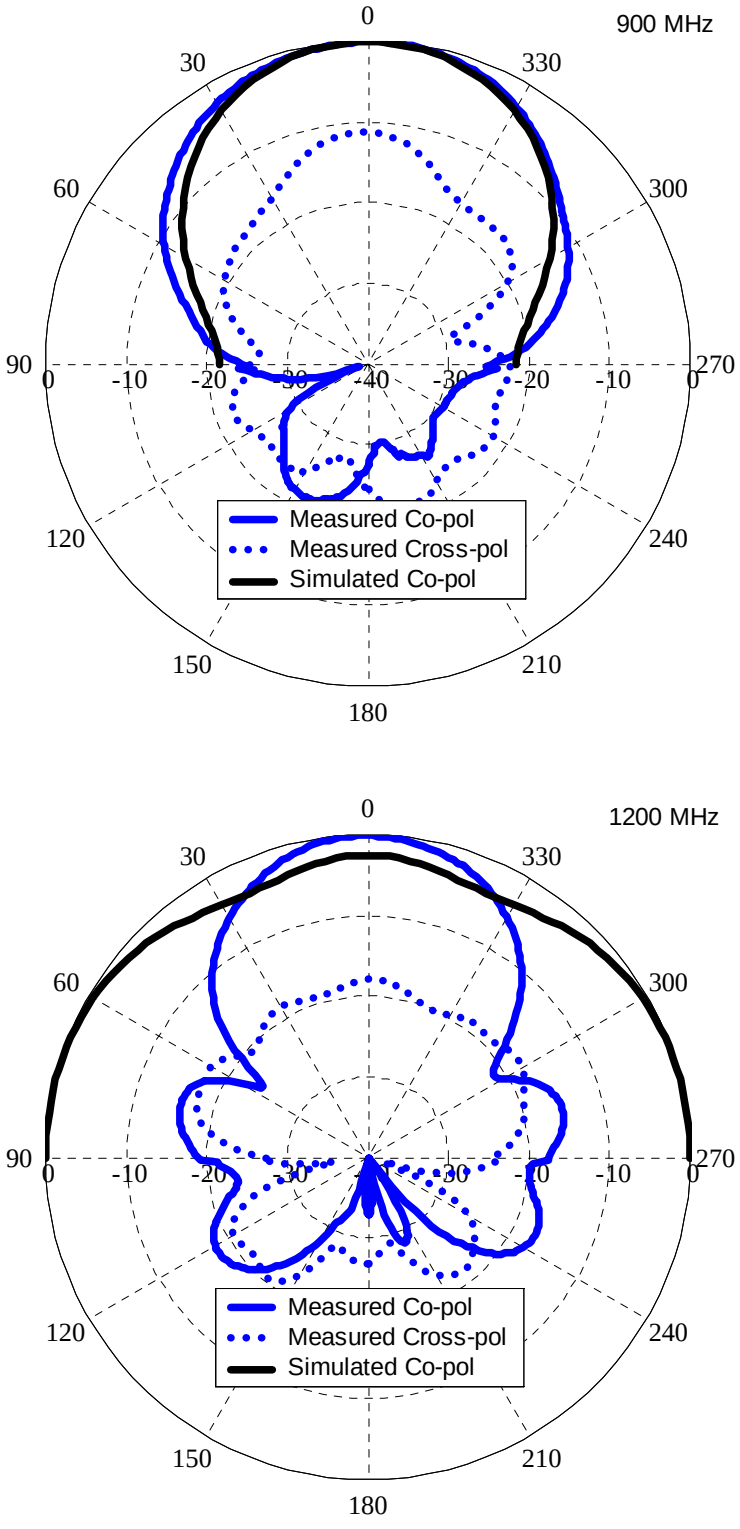

Figure 5.20 Comparison of measured radiation patterns to simulated data for 7-element WAVES array of Fig. 5.15. Theta cuts. $\phi = 0°$.

Note: The disagreement seen at 1200 MHZ is due to numerical error.

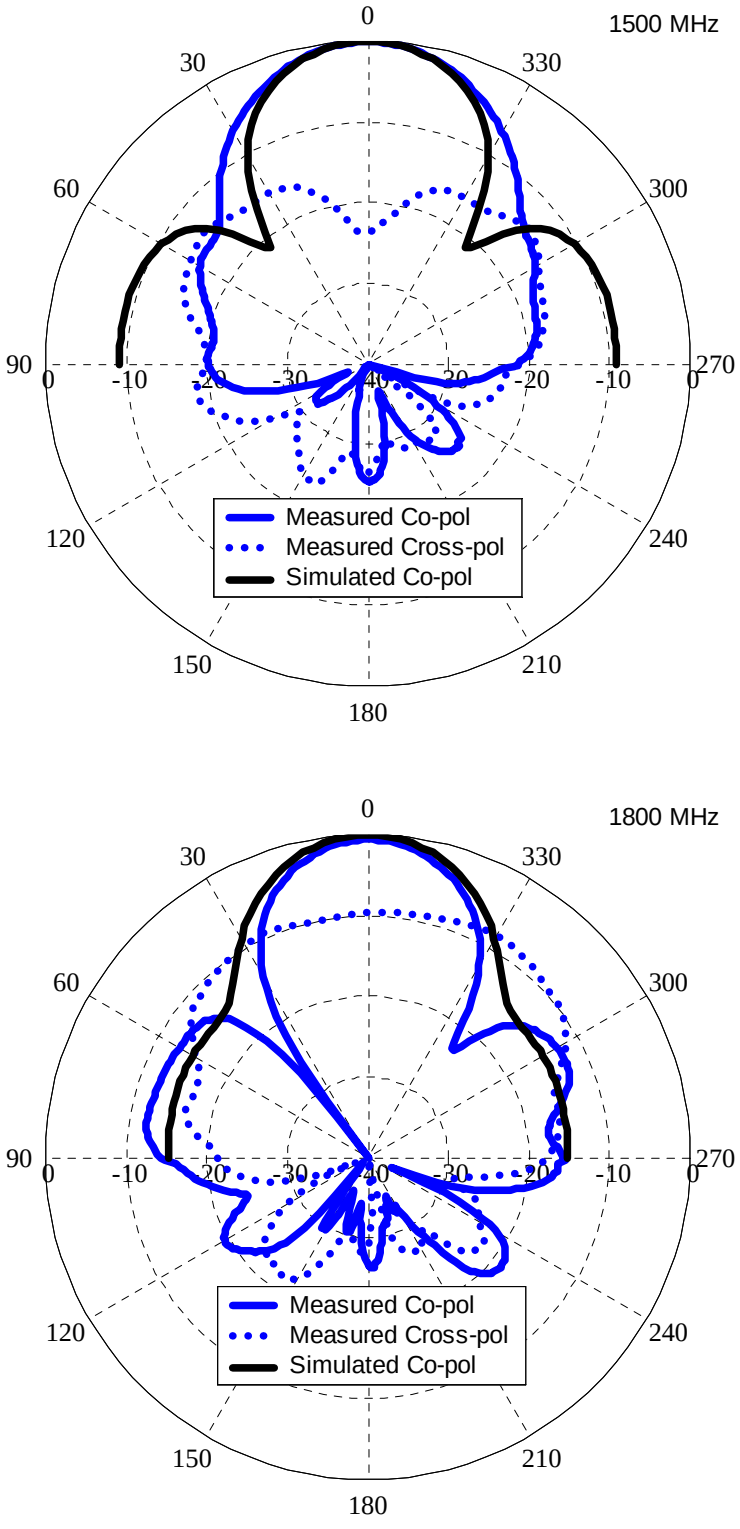

Figure 5.20 (cont) Comparison of measured radiation patterns to simulated data for 7-element WAVES array of Fig. 5.15. Theta cuts. $\phi = 0°$.

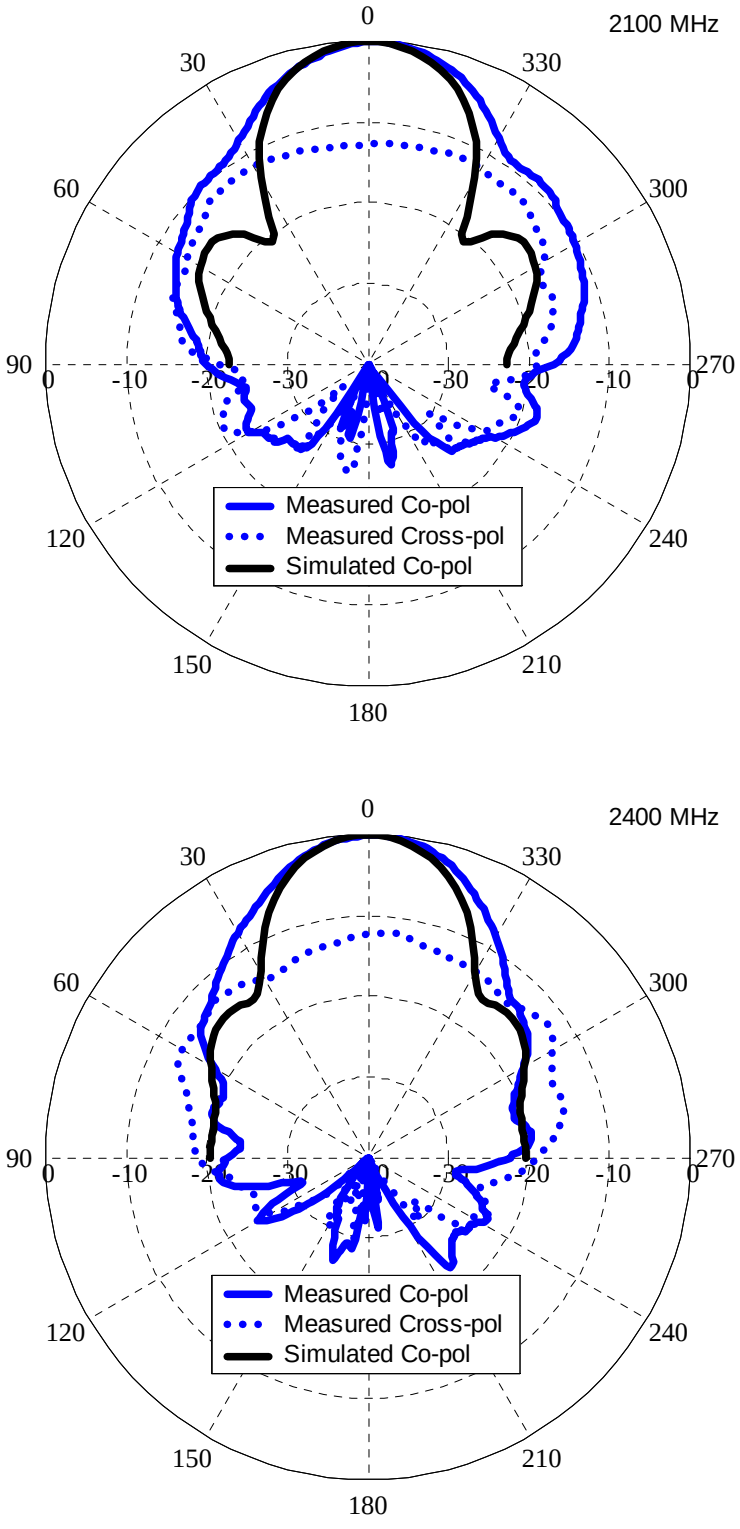

Figure 5.20 (cont) Comparison of measured radiation patterns to simulated data for 7-element WAVES array of Fig. 5.15. Theta cuts. $\phi = 0°$.

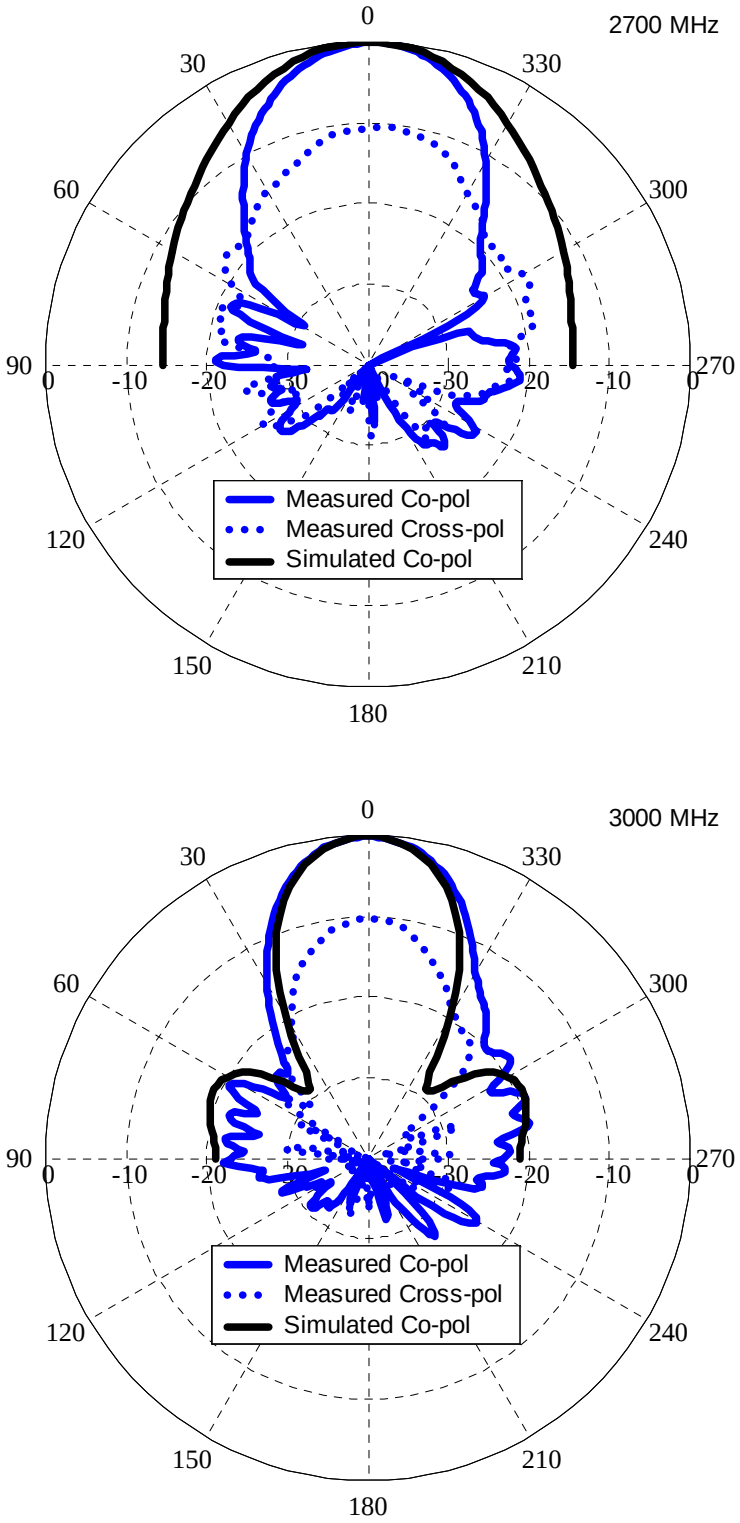

Figure 5.20 (cont) Comparison of measured radiation patterns to simulated data for 7-element WAVES array of Fig. 5.15. Theta cuts. $\phi = 0°$.

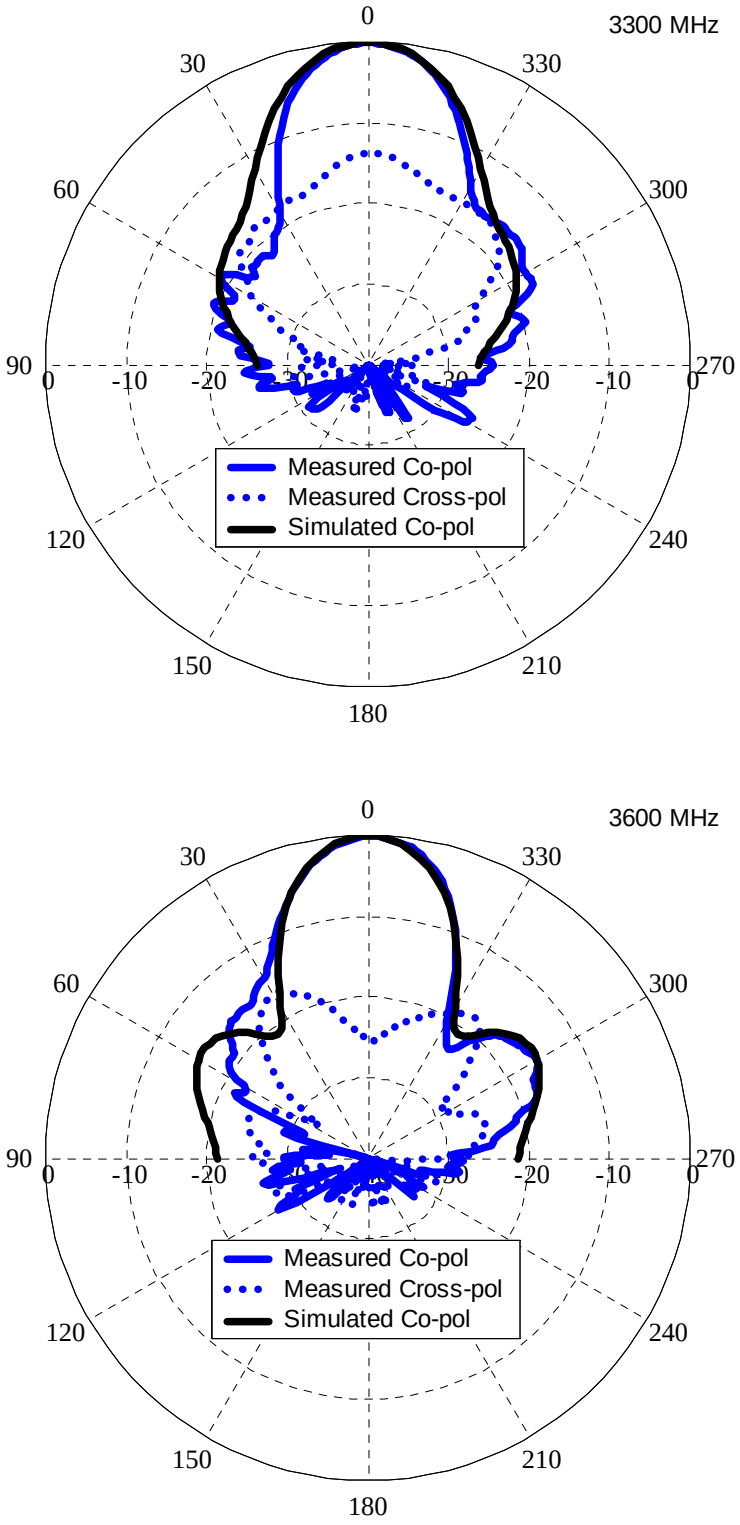

Figure 5.20 (cont) Comparison of measured radiation patterns to simulated data for 7-element WAVES array of Fig. 5.15. Theta cuts. $\phi = 0°$.

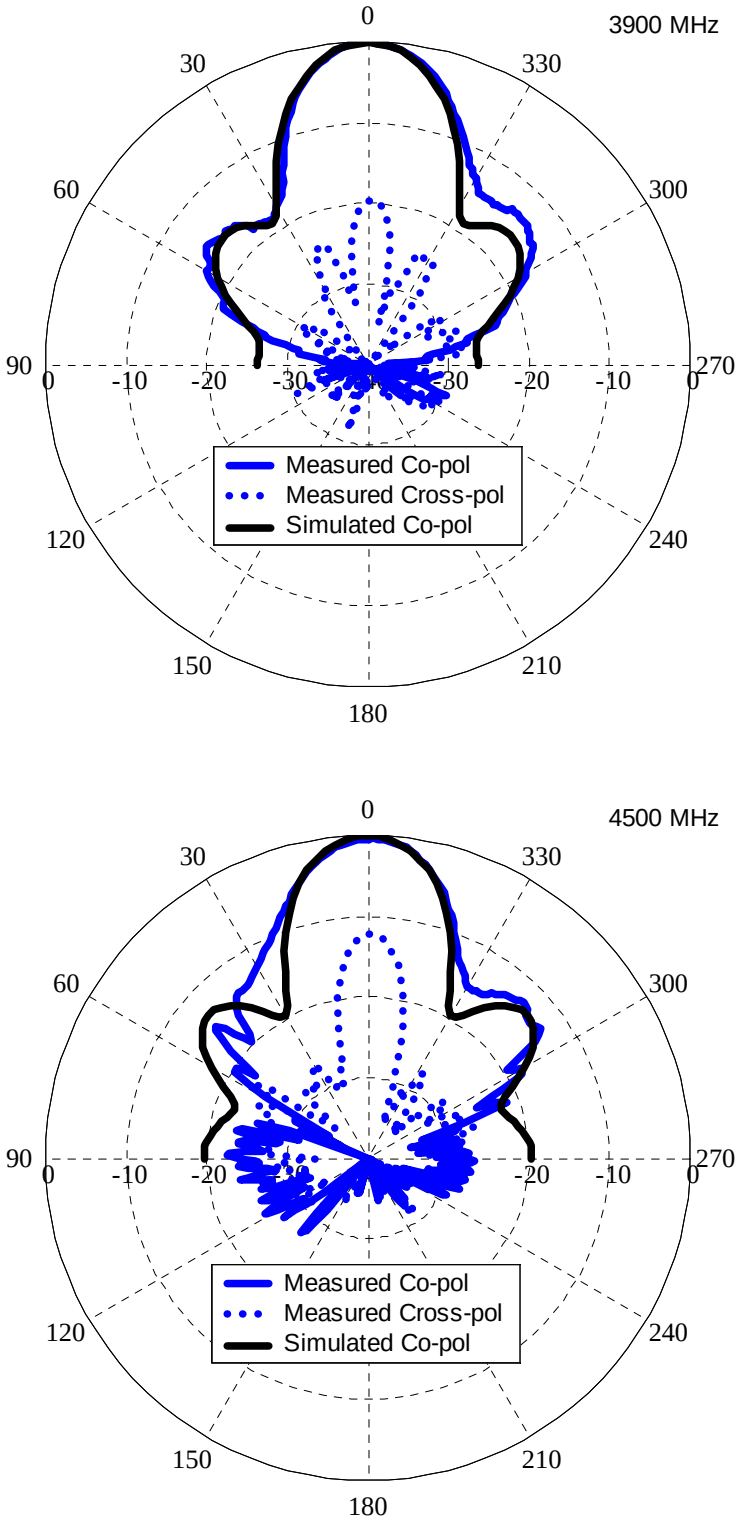

Figure 5.20 (cont) Comparison of measured radiation patterns to simulated data for 7-element WAVES array of Fig. 5.15. Theta cuts. $\phi = 0°$.

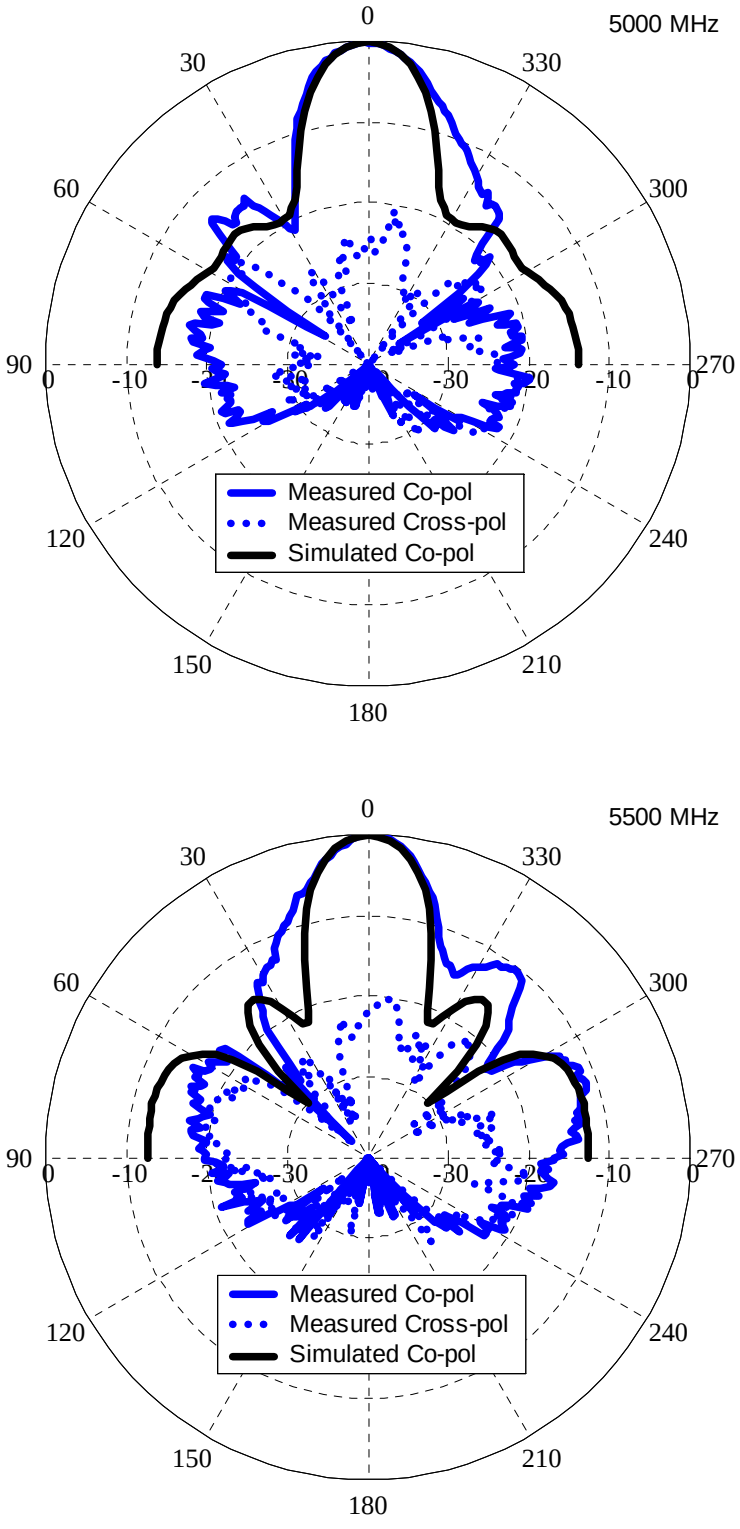

Figure 5.20 (cont) Comparison of measured radiation patterns to simulated data for 7-element WAVES array of Fig. 5.15. Theta cuts. $\phi = 0°$.

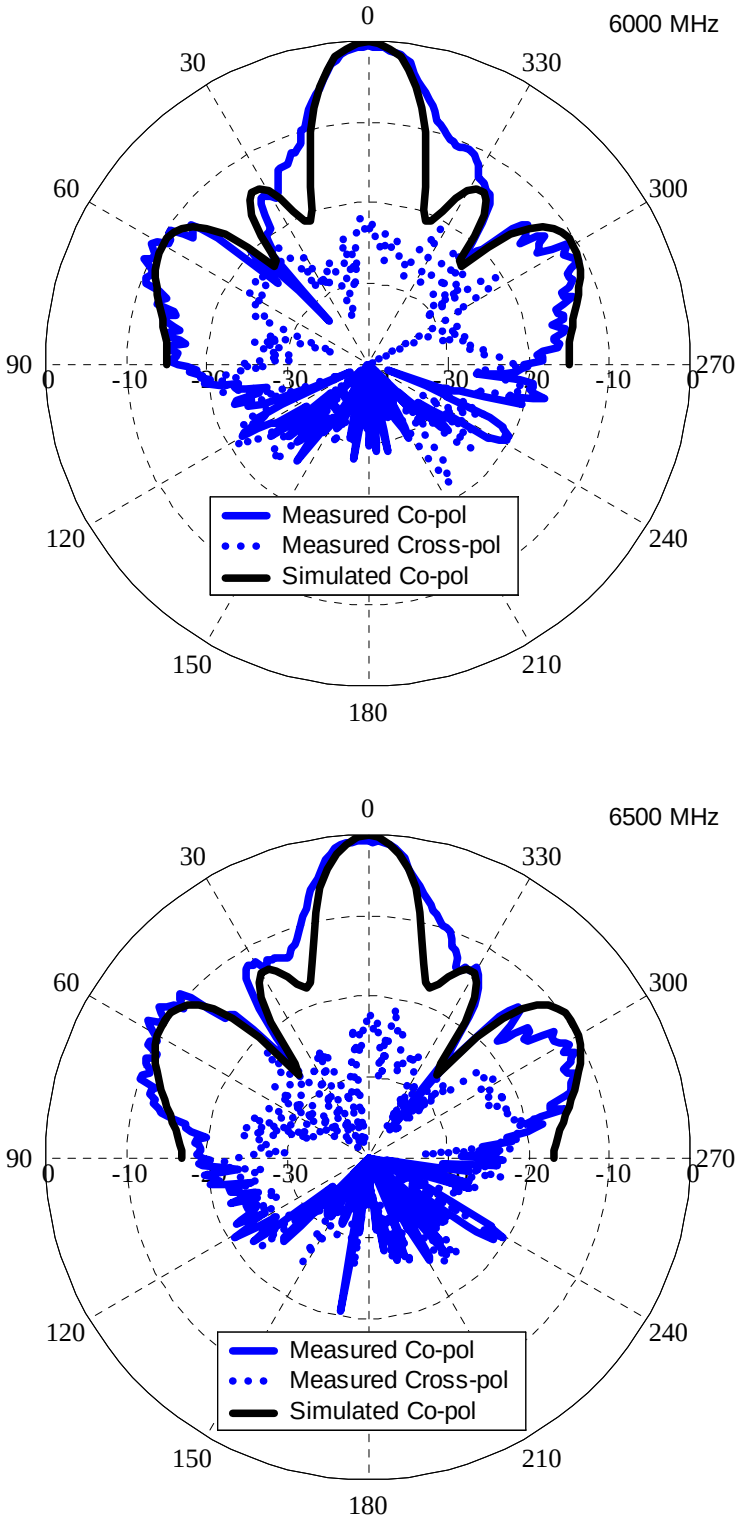

Figure 5.20 (cont) Comparison of measured radiation patterns to simulated data for 7-element WAVES array of Fig. 5.15. Theta cuts. $\phi = 0°$.

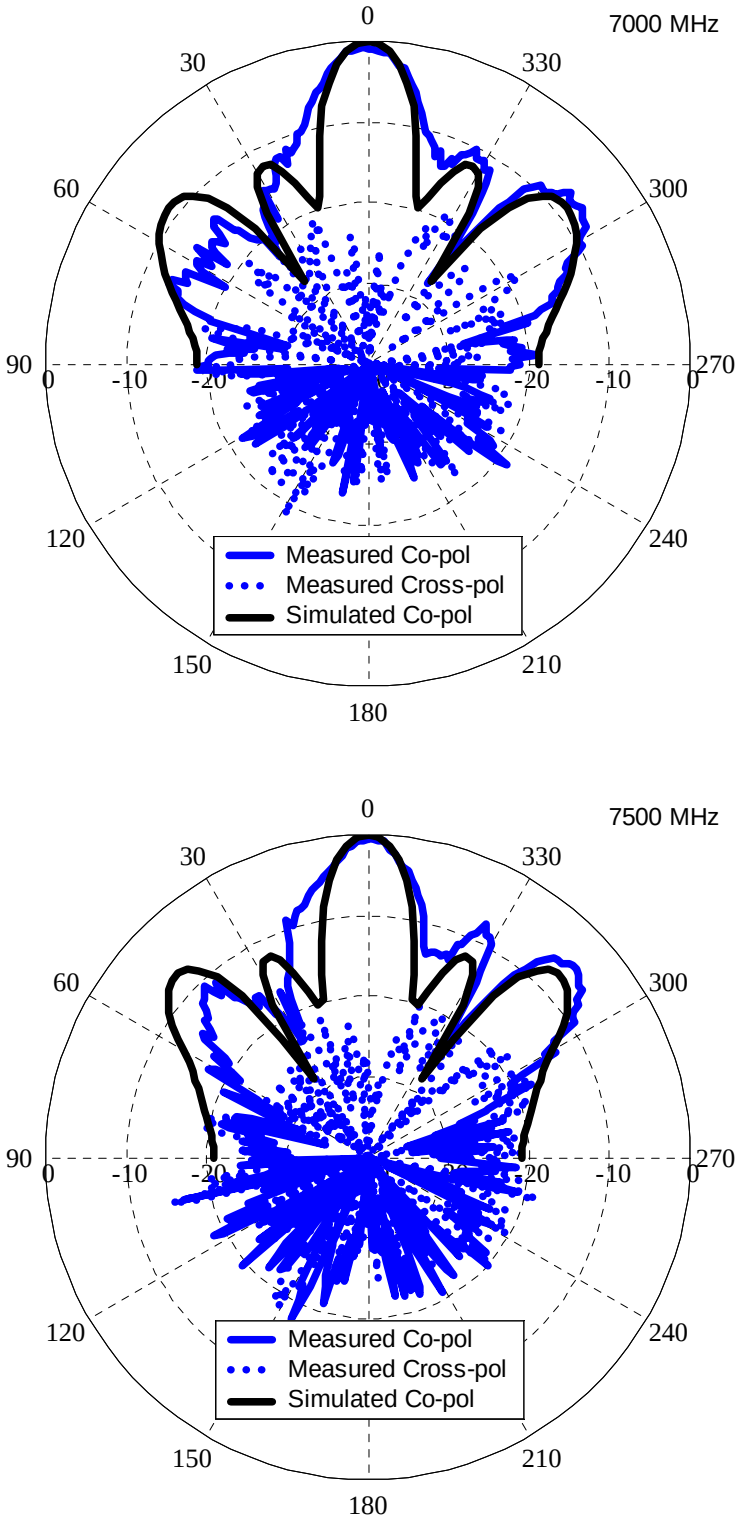

Figure 5.20 (cont) Comparison of measured radiation patterns to simulated data for 7-element WAVES array of Fig. 5.15. Theta cuts. $\phi = 0°$.

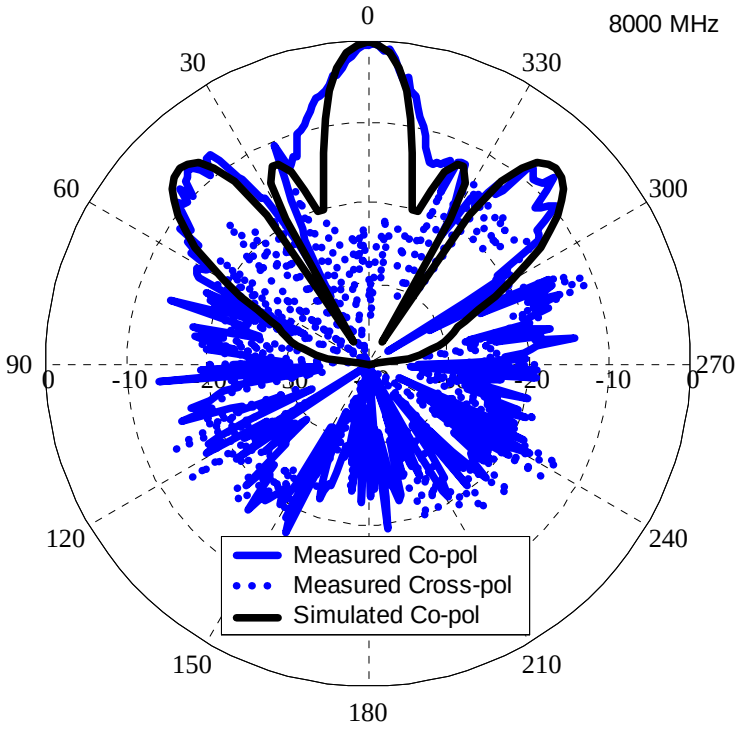

Figure 5.20 (cont) Comparison of measured radiation patterns to simulated data for 7-element WAVES array of Fig. 5.15. Theta cuts. $\phi = 0°$.

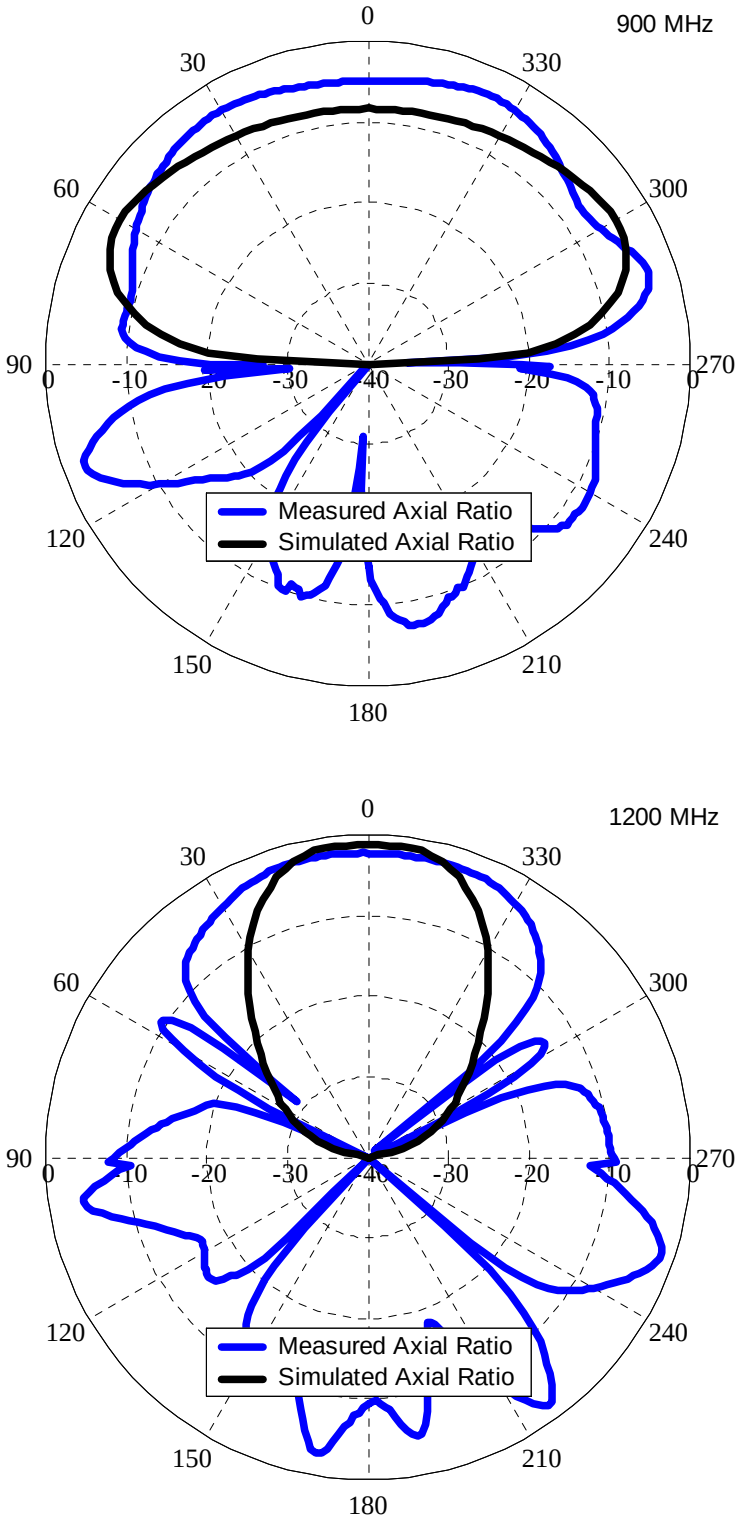

Figure 5.21 Comparison of measured axial ratio to simulated data for 7-element WAVES array of Fig. 5.15. Theta cuts. $\phi = 0°$.

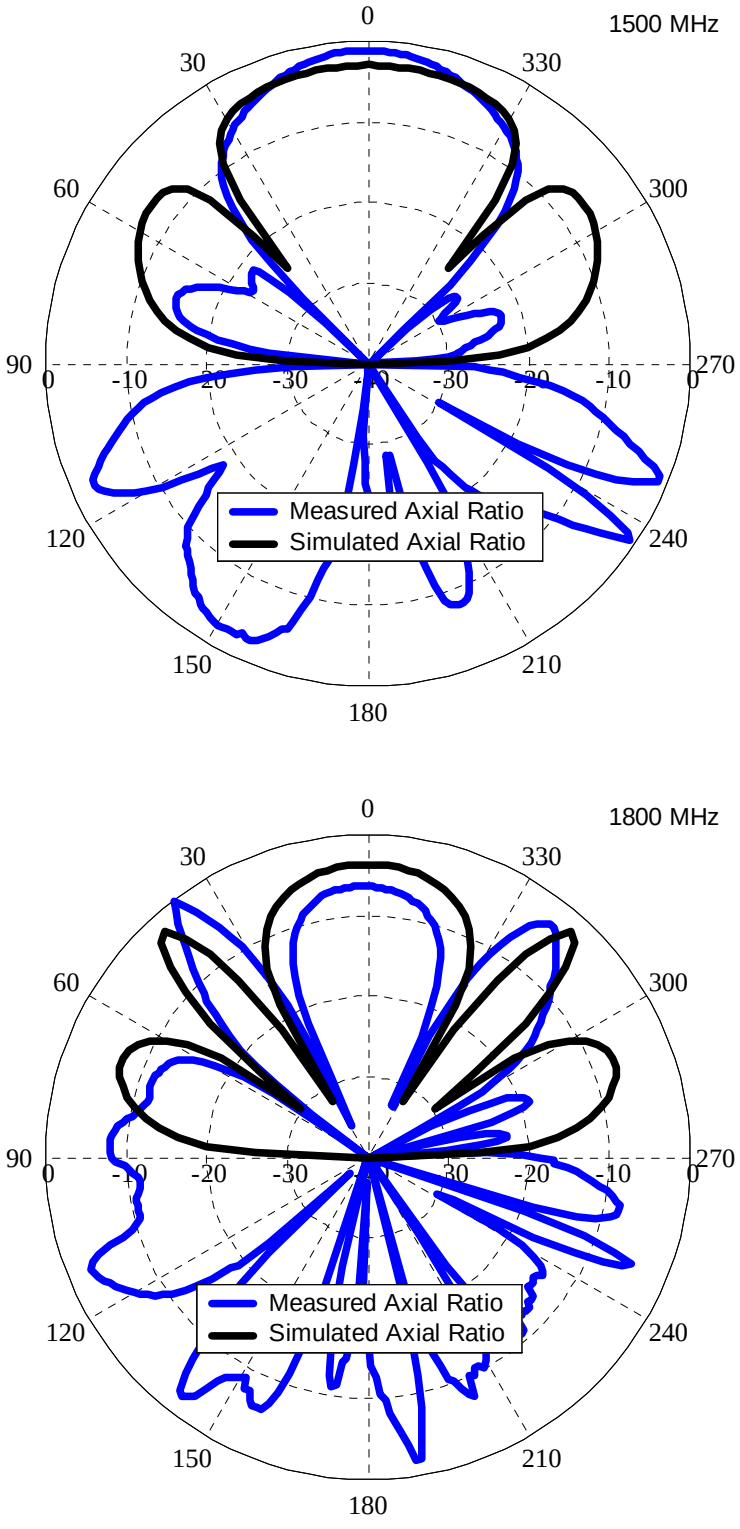

Figure 5.21 (cont) Comparison of measured axial ratio to simulated data for 7-element WAVES array of Fig. 5.15. Theta cuts. $\phi = 0°$.

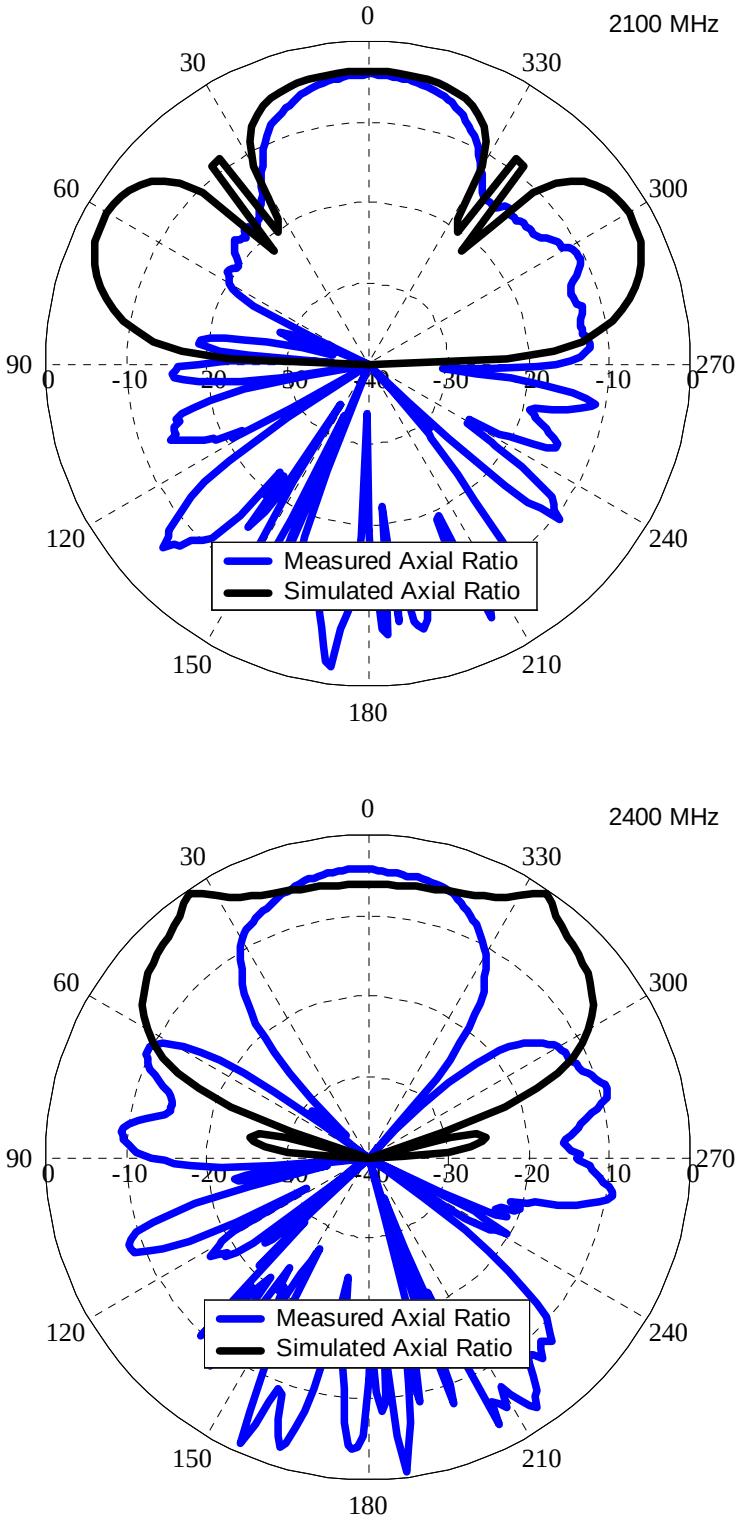

Figure 5.21 (cont) Comparison of measured axial ratio to simulated data for 7-element WAVES array of Fig. 5.15. Theta cuts. $\phi = 0°$.

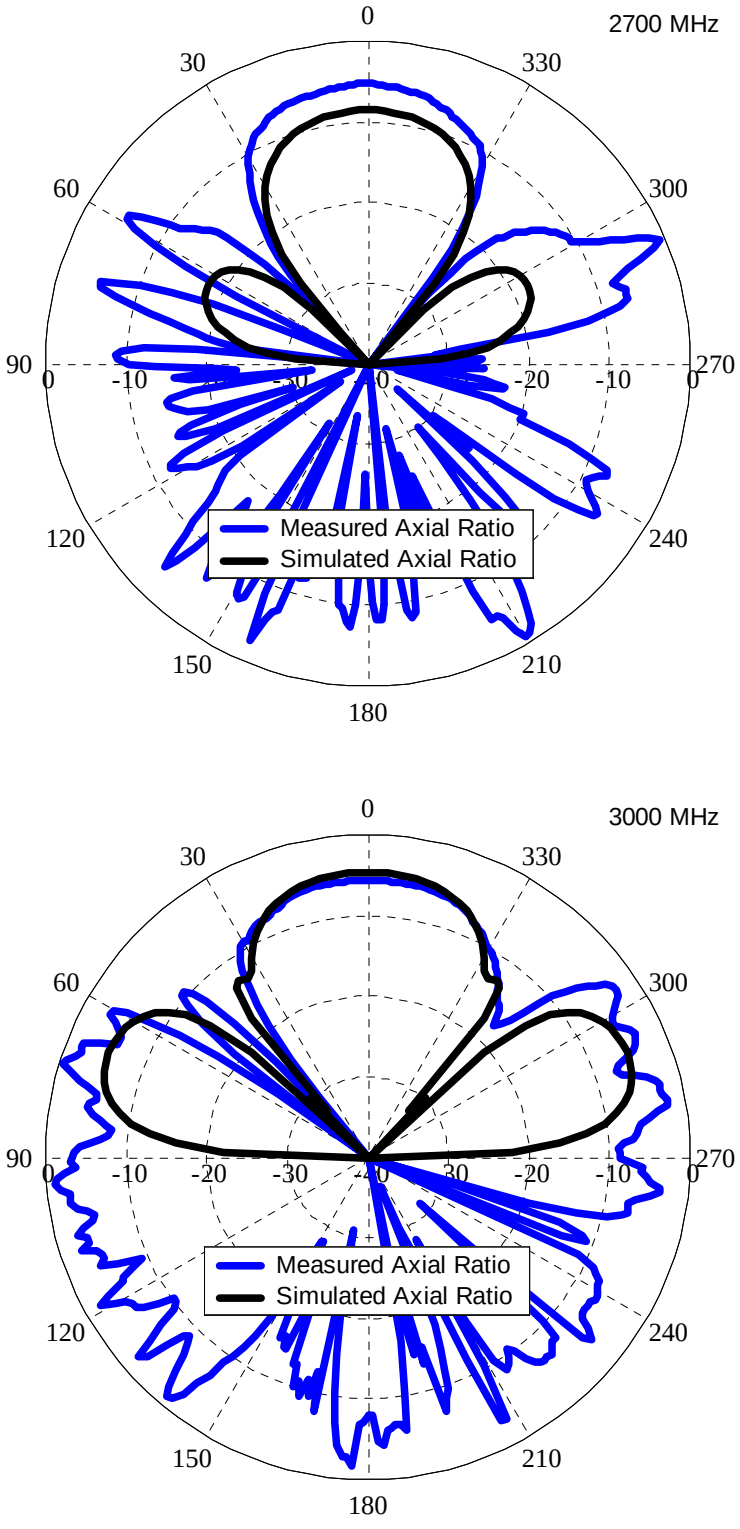

Figure 5.21 (cont) Comparison of measured axial ratio to simulated data for 7-element WAVES array of Fig. 5.15. Theta cuts. $\phi = 0°$.

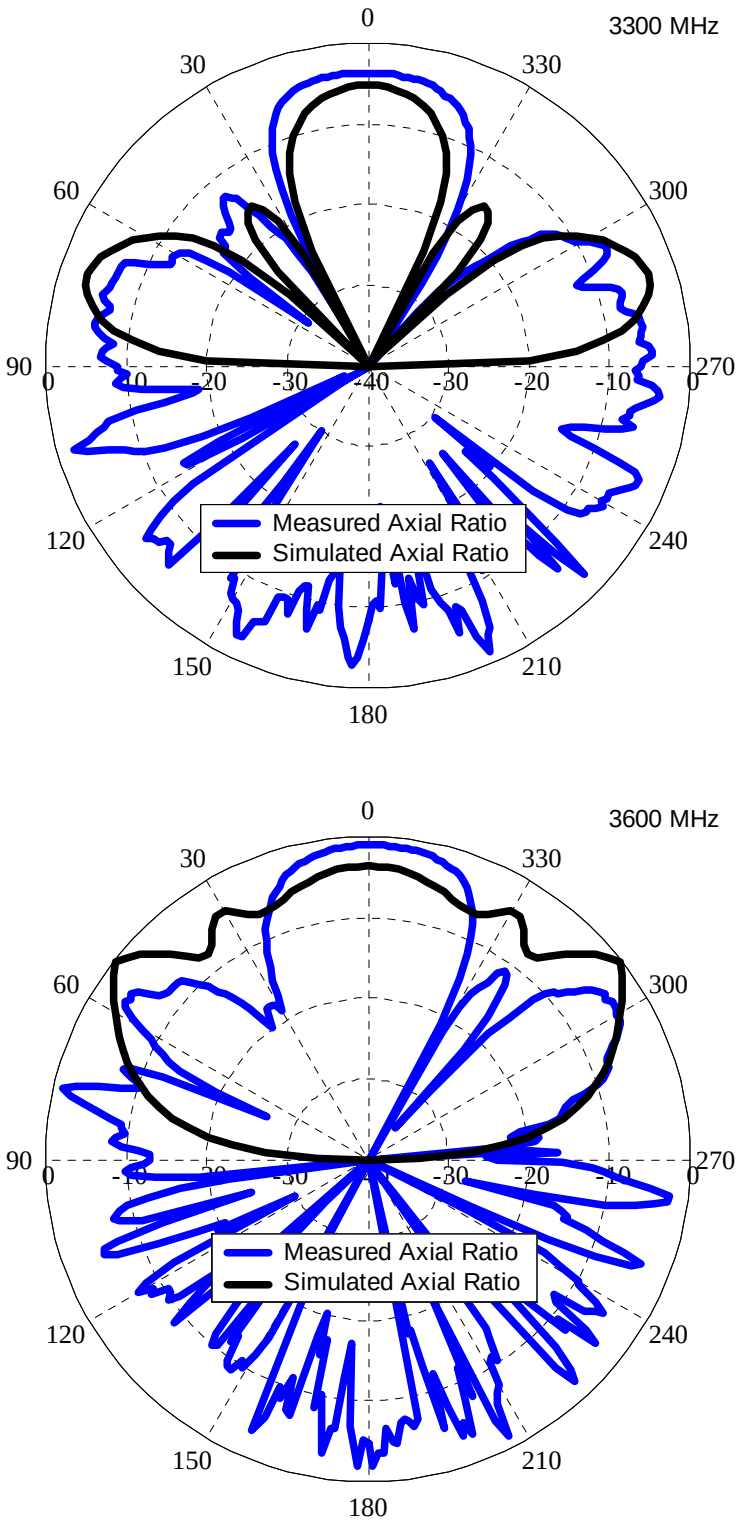

Figure 5.21 (cont) Comparison of measured axial ratio to simulated data for 7-element WAVES array of Fig. 5.15. Theta cuts. $\phi = 0°$.

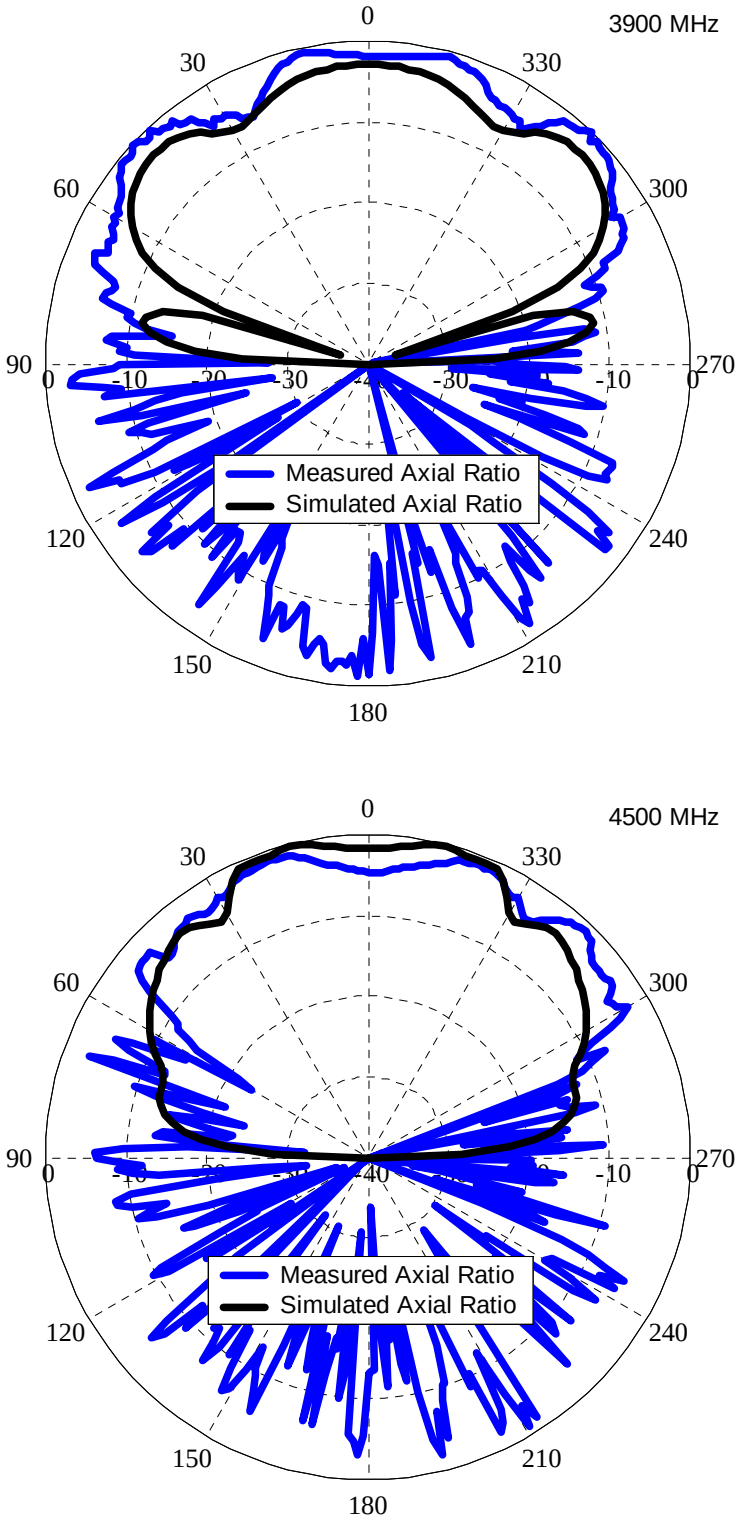

Figure 5.21 (cont) Comparison of measured axial ratio to simulated data for 7-element WAVES array of Fig. 5.15. Theta cuts. $\phi = 0°$.

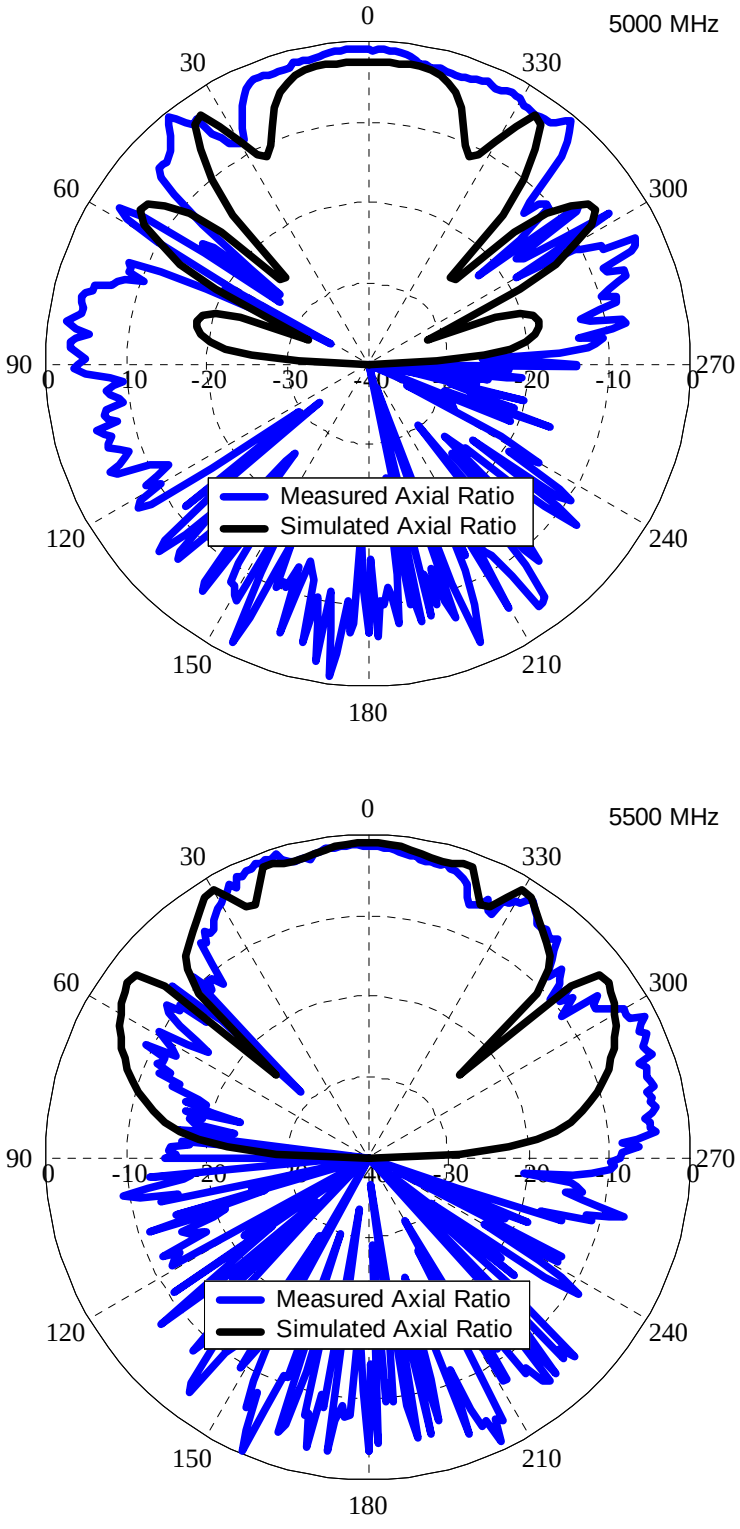

Figure 5.21 (cont) Comparison of measured axial ratio to simulated data for 7-element WAVES array of Fig. 5.15. Theta cuts. $\phi = 0°$.

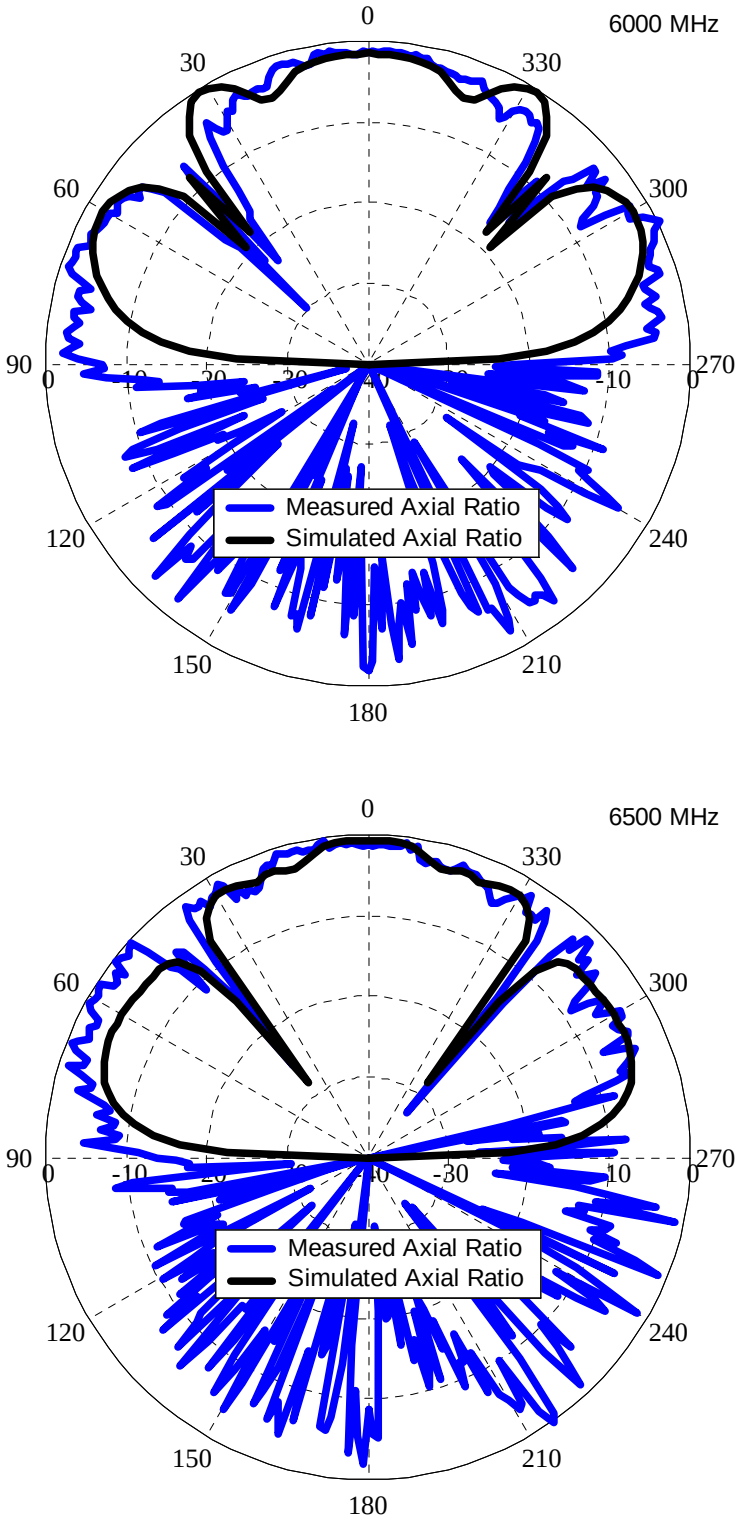

Figure 5.21 (cont) Comparison of measured axial ratio to simulated data for 7-element WAVES array of Fig. 5.15. Theta cuts. $\phi = 0°$.

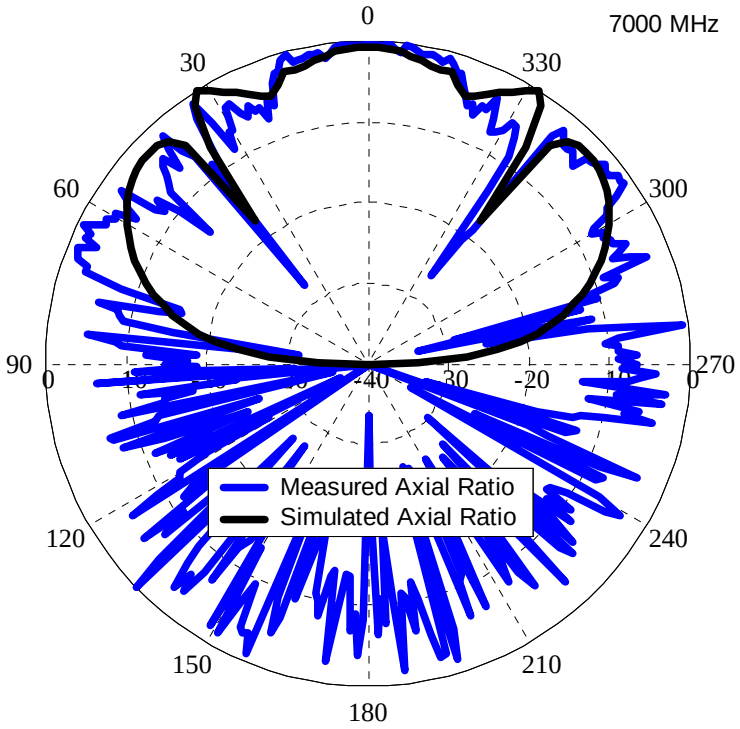

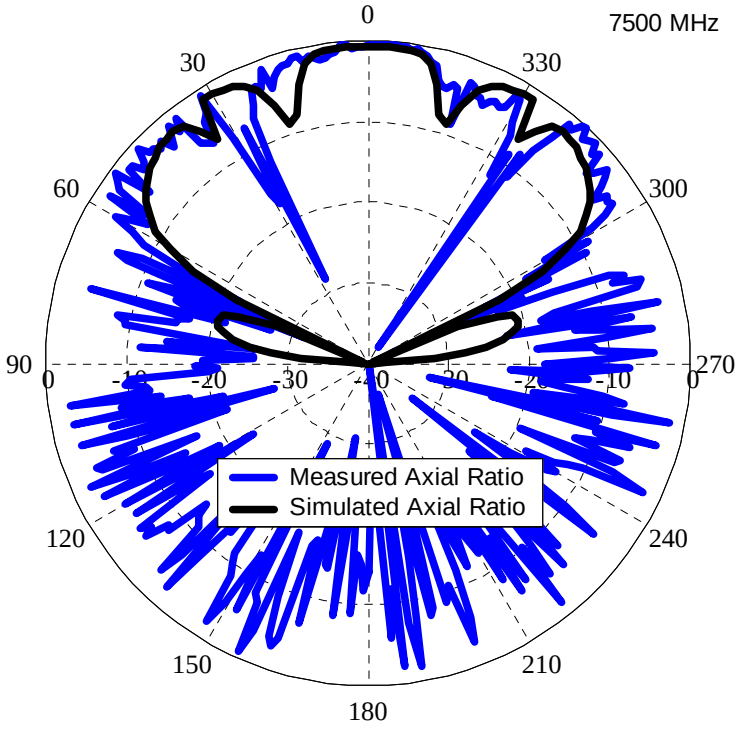

Figure 5.21 (cont) Comparison of measured axial ratio to simulated data for 7-element WAVES array of Fig. 5.15. Theta cuts. $\phi = 0°$.

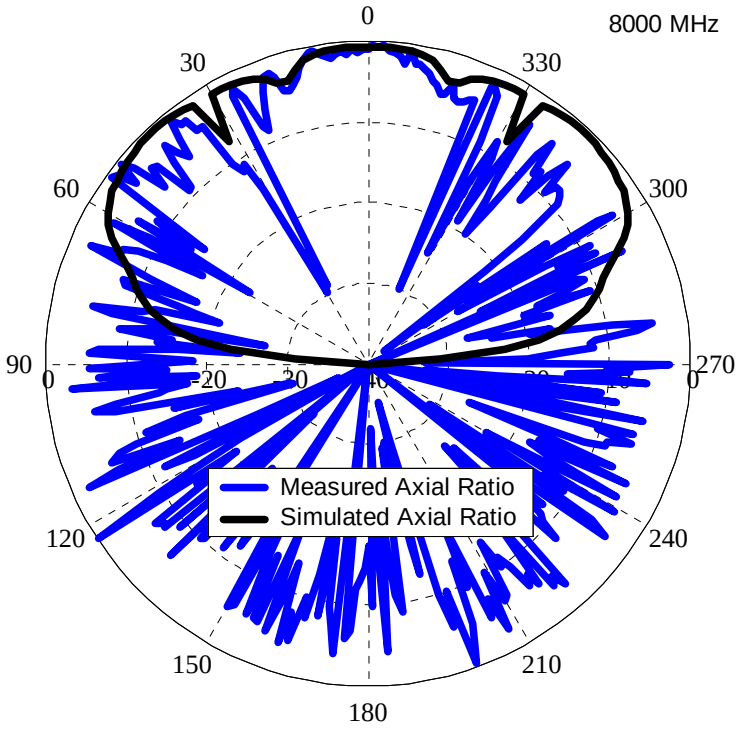

Figure 5.21 (cont) Comparison of measured axial ratio to simulated data for 7-element WAVES array of Fig. 5.15. Theta cuts. $\phi = 0°$.

5.4 Scan Performance of 3-Octave WAVES Array

The previous section demonstrated that a 3-octave WAVES array is feasible. It also further validated the NEC4 simulations that have been used throughout this thesis. This section will provide an initial feasibility study of the scan performance of a WAVES array through simulations. For many applications, satisfactory scan performance is essential for the WAVES array to be considered as an alternative to a reflector antenna system, unless mechanical steering is to be considered. The array geometry and setup is the same as Fig. 5.14. The gain loss of the 3-octave WAVES array of star spirals is shown in Fig. 5.22. The gain loss is an indicator of how the mutual coupling between elements changes with scan angle. The gain loss is relatively minor for all of the frequencies chosen, but there is a definite trend of improved performance with increasing frequency. This is probably due to the nature of spiral antennas. At the lower frequencies, the active region of the spirals is closer to the outer dimension of the spirals, which increases the interaction between them.

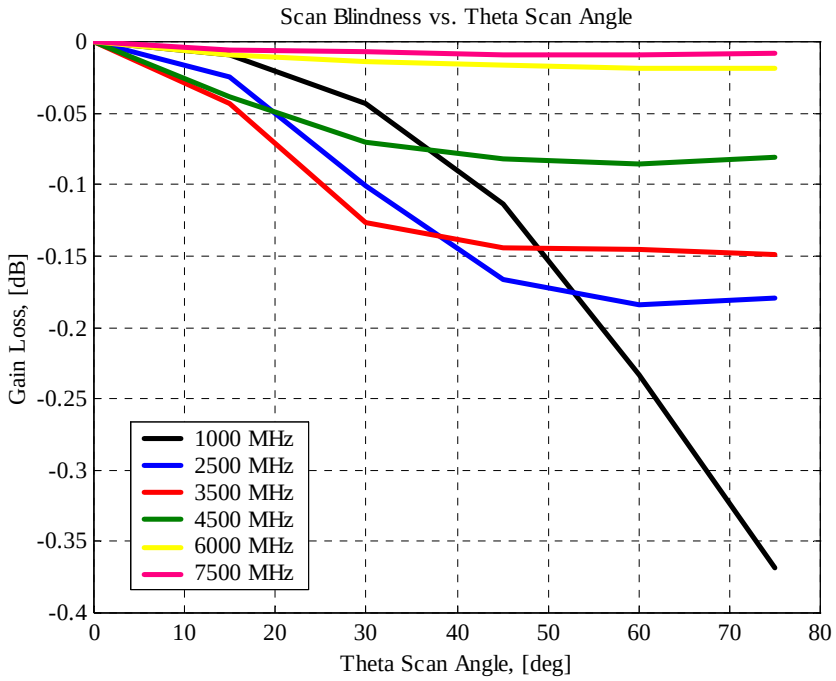

Figure 5.22 Comparison of gain loss versus theta scan angle at selected frequencies for the 3-octave WAVES array of star spirals.

The gain loss does not tell the whole story. It is also necessary to look at the actual patterns as the beam is scanned. Typically, if the WAVES array was used in a practical system, the array would be much larger and the main beam of the array would be much more defined. However, since this is a preliminary feasibility study, the small 3-octave WAVES array of the previous section is suitable for studying some general trends. The scanned array patterns for the array at the selected frequencies are plotted in Fig. 5.23. The general trend seen in the scanned patterns is for the main beam peak to decrease and the side and back lobes to increase with increasing theta scan angle. This effect becomes more pronounced with increasing frequency because the grating lobes start to appear. The array seems to scan well up to about 45° for frequencies less than 4500 MHz. At the higher frequencies the grating lobes begin to dominate the pattern, but the array still scans moderately well up to about 30°. As stated above, it is expected that the scan performance would improve for a larger array. Also, this is just a feasibility study using the 3-octave array that was previously introduced in this chapter. The scan performance can probably be greatly improved through future research and development.

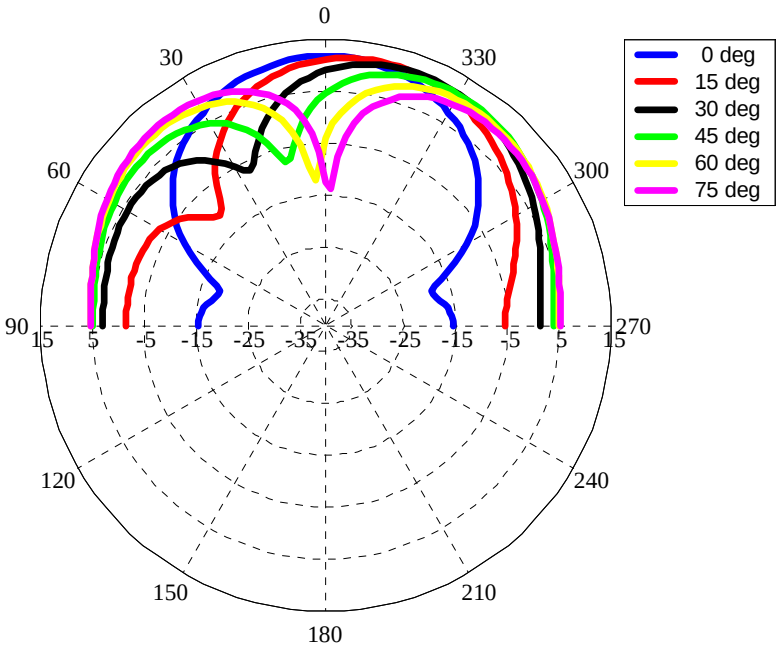

(a) 1000 MHz

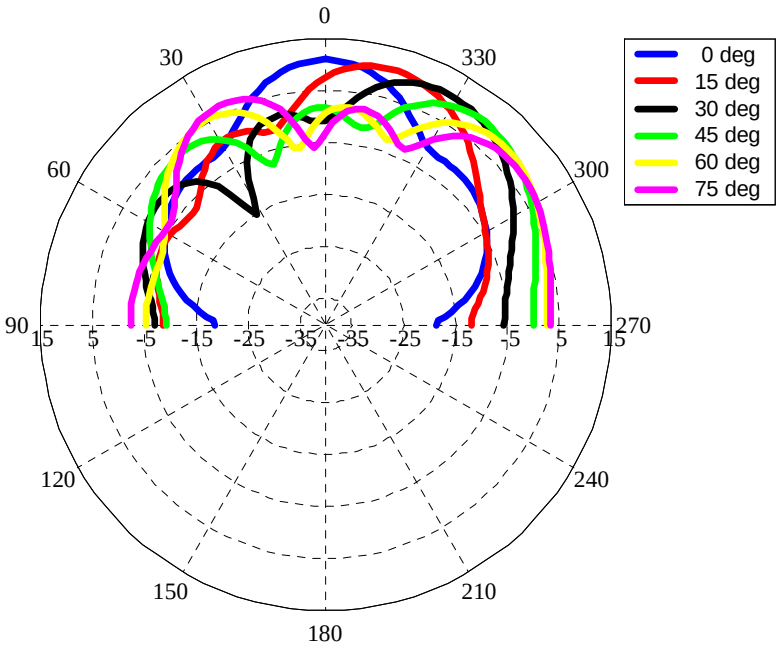

(c) 2500 MHz

Figure 5.23 Scanned array patterns for 3-octave WAVES array of star spirals.

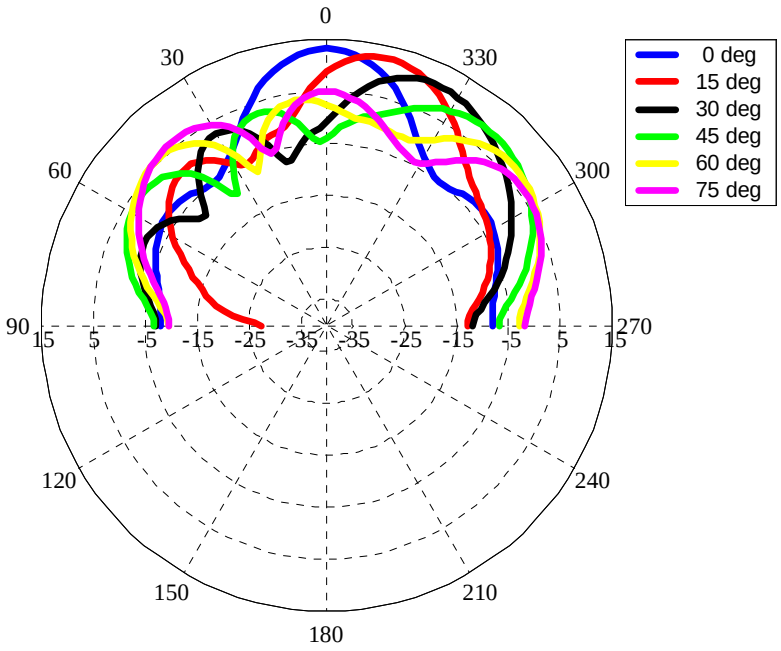

(d) 3500 MHz

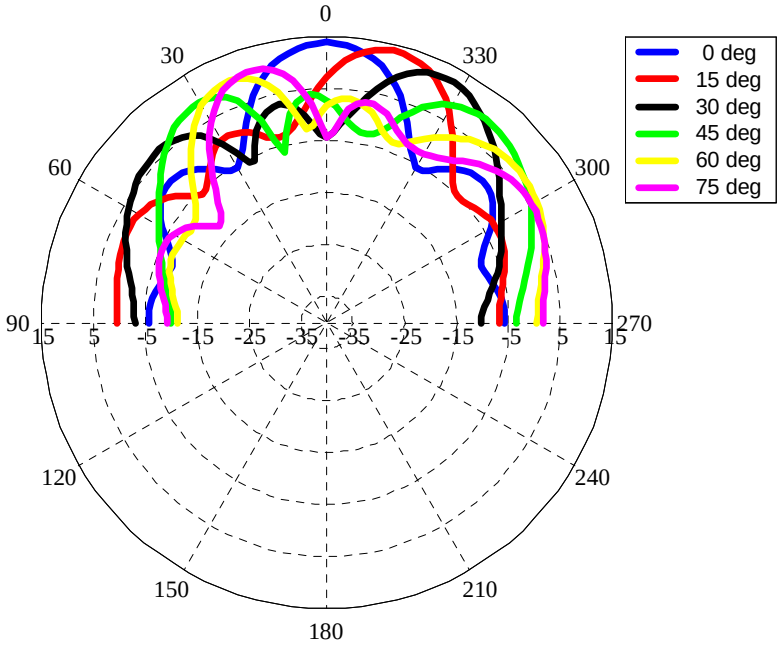

(e) 4500 MHz

Figure 5.23 (cont) Scanned array patterns for 3-octave WAVES array of star spirals.

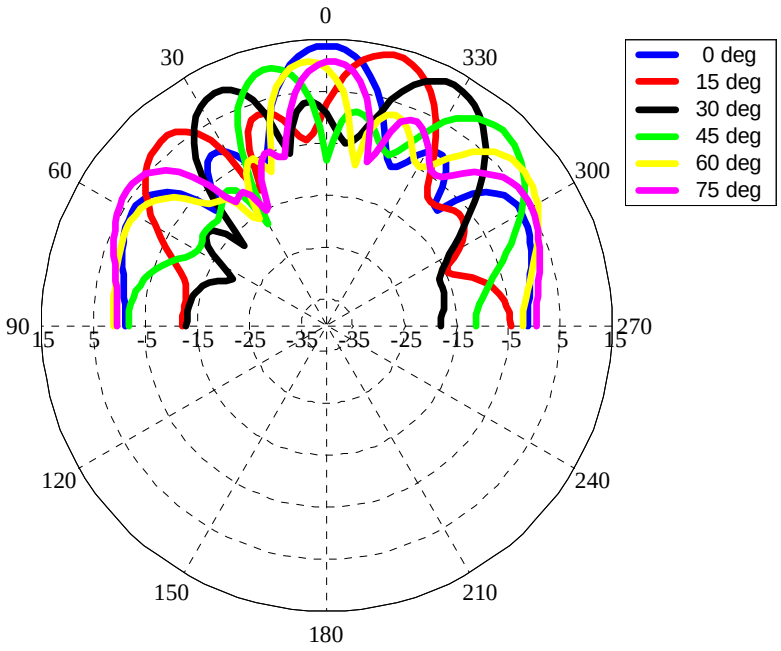

(f) 6000 MHz

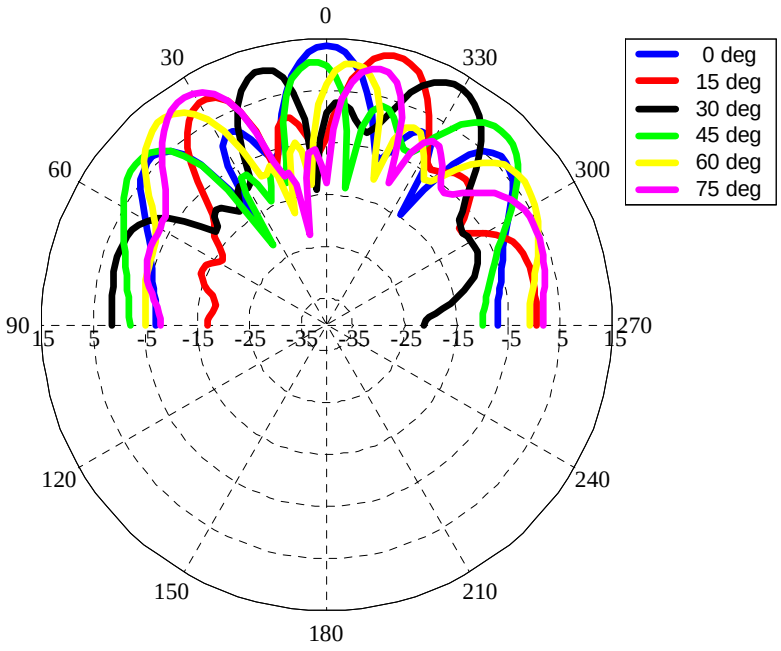

(g) 7500 MHz

Figure 5.23 (cont) Scanned array patterns for 3-octave WAVES array of star spirals.

5.5 Alternative WAVES Array Geometries

The unique array packing features of the star spiral were demonstrated in Section 5.2 for the linear WAVES array. There are many other geometries that can take advantage of the improved array packing of the star spiral. Some of these arrays will be presented in this section. This section is only intended to show some alternative arrays, not to provide a full analysis of each geometry. A 2-octave planar, circular WAVES array geometry is shown in Fig. 5.24. The inter-element spacing of the array is smaller

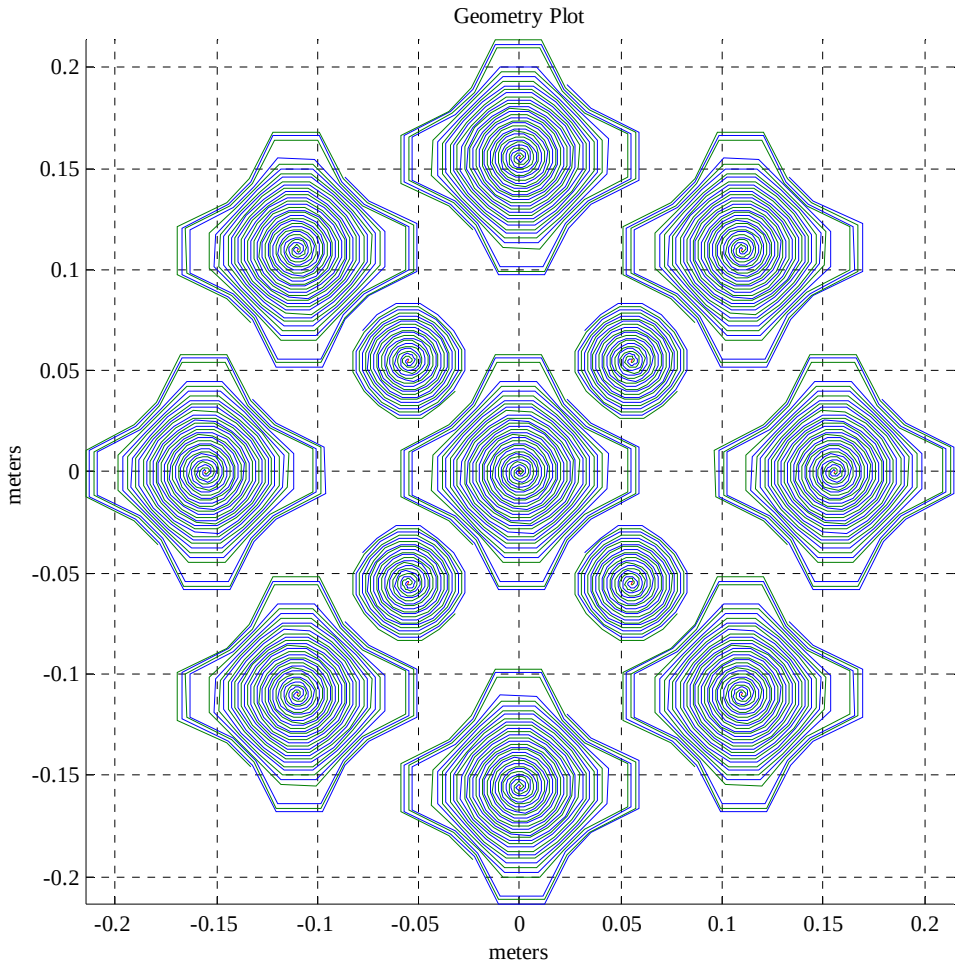

Figure 5.24 Alternative 2-octave planar, circular WAVES array of star spirals.

than the linear WAVES array presented earlier in this chapter and the array has an amplitude taper that should help with grating lobes. This array should yield improved scan performance since the inter-element spacing is reduced over the linear array. The circular array can also be extended to cover 3-octaves as seen in Fig. 5.25. The 3-octave array would probably be more effective if it were made larger. The 3-octave array measured earlier in this chapter can be easily extended to become a planar array as shown in Fig. 5.26. Note that if circular or square spirals were used in the array geometries shown here that some of the spirals would overlap. A few possible array geometries have been presented, but many additional geometries are possible that make use of the packing provided by the star spiral.

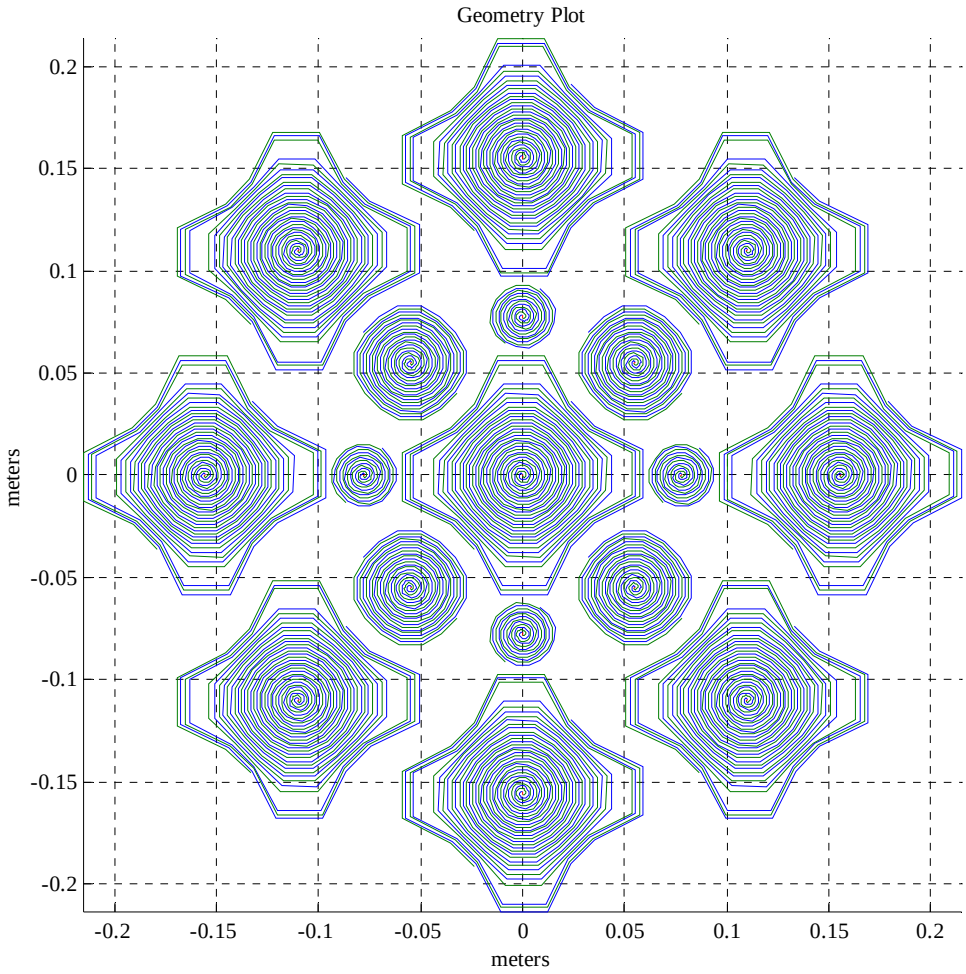

Figure 5.25 Alternative 3-octave planar, circular WAVES array of star spirals.

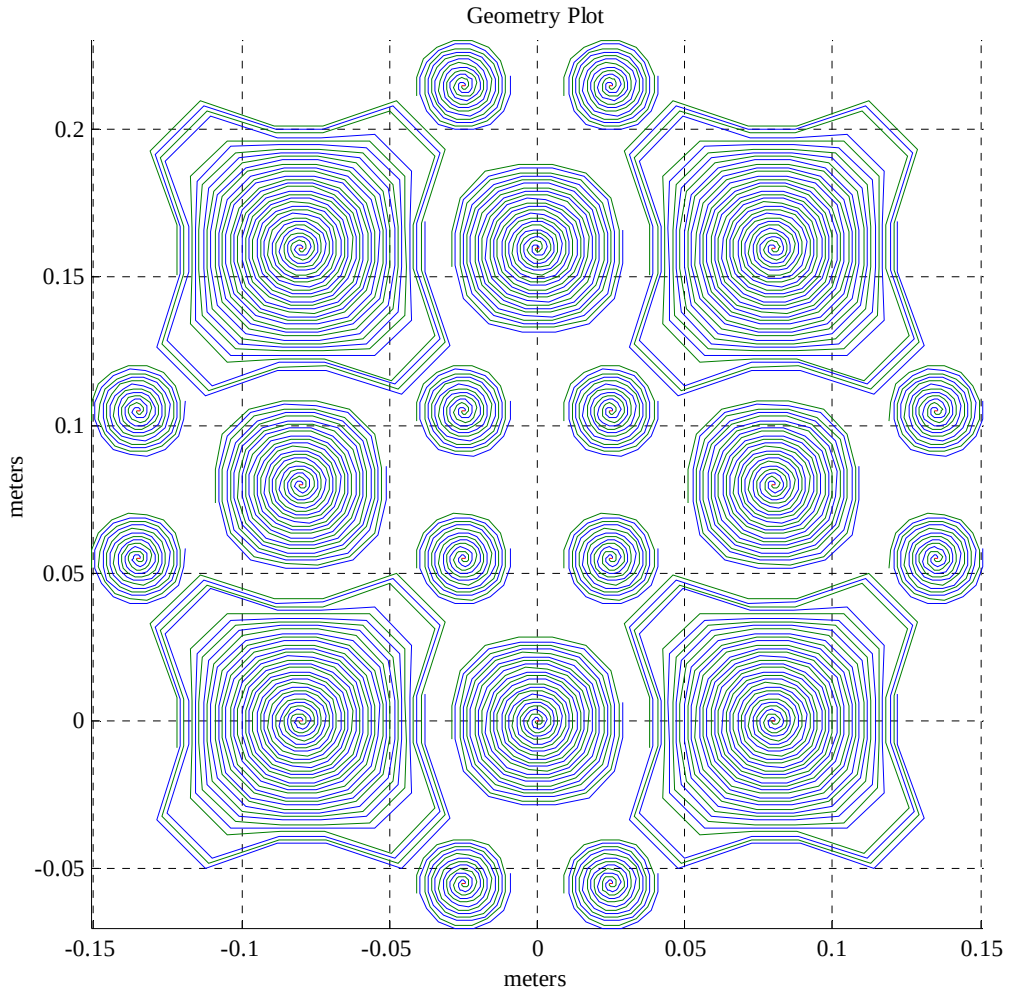

Figure 5.26 Planar extension of 3-octave WAVES array of star spirals measured in Section 5.3.

5.6 Summary

The performance of the star spiral in an array environment has been investigated in this chapter. An infinite array of star spirals was compared to an infinite array of circular Archimedean spirals. The comparison showed that the unique shape of the star spiral did not significantly affect the scan performance of the infinite array. It was also shown that the size reduction and shape of the star spiral allowed for the elimination of the performance gap observed in the linear WAVES array of circular spirals in Chapter 3.

Measurements were performed on a simple 3-octave WAVES array of star spirals. Greater than 3 octaves of coverage were demonstrated and validated by both measurements and simulations. An initial feasibility study of the scan performance of a WAVES array was also studied. The results show the potential of the WAVES array to provide adequate scan performance, particularly for larger arrays than were considered in this thesis. Finally, a few possible alternative array geometries were presented. The results of the 3-octave array presented will improve if the size of the array is increased such as in Fig. 5.26. The increased number of elements and amplitude taper provided by the larger array should improve side lobes and scan performance of the array.